Theory of Edge Radiation.

Part I: foundations and basic applications

Gianluca Geloni, [1] Vitali Kocharyan, Evgeni Saldin,

Evgeni Schneidmiller and Mikhail Yurkov

Deutsches Elektronen-Synchrotron (DESY), Hamburg, Germany

Abstract

We formulate a complete theory of Edge Radiation based on a novel method relying on Fourier Optics techniques. Special attention is payed in discussing the validity of approximations upon which the theory is built. Our study makes consistent use of both similarity techniques and comparisons with numerical results from simulation. We discuss both near and far zone. Physical understanding of many asymptotes is discussed. As an example of application we discuss the case of Transition Undulator Radiation, which can be conveniently treated with our formalism.

Key words:

edge radiation, near-field, undulator transition radiation

PACS: 41.60.Cr, 42.25.-p, 41.75.-Ht

[1] Corresponding Author. Tel: ++49 40 8998 5450. Fax: ++49 40 8998 1905. E-mail address: gianluca.aldo.geloni@desy.de

Preprint submitted to *26 March 2009*

1 Introduction

Synchrotron Radiation (SR) sources from bending magnets are brilliant, and cover the continuous spectral range from microwaves to X-rays. However, in order to optimally meet the needs of basic research with SR, it is desirable to provide specific radiation characteristics, which cannot be obtained from bending magnets, but require special magnetic setups, called insertion devices. These are installed along the particle beam path between two bending magnets, and introduce no net beam deflection. Therefore, they can be incorporated in a given beamline without changing its geometry. Undulators are a typical example of such devices, generating specific radiation characteristics in the short wavelength range.

The history of SR utilization in the long wavelength region (from micrometer to millimeter) is more recent than that in the short wavelength range. Long wavelength SR sources may have a strong potential for infrared spectroscopy or imaging techniques. In fact, they are some order of magnitude brighter than standard thermal sources in the same spectral range.

Large angles are required to extract long wavelength SR from bending magnets, because the ”natural” opening angle in this case increases up to several tens milliradians in the far-infrared range. However, the situation changes dramatically if a straight section is introduced between two bends, like in Fig. 1(a). Long-wavelength radiation emitted by relativistic electrons in this setup is called Edge Radiation (ER), and presents a significantly smaller opening angle than standard SR from bends (see, among others, [1]-[14]). In other words, in the long wavelength region (compared to the critical bending-magnet radiation wavelength) a simple straight section between bends can play the role of a kind of insertion device.

ER and bending magnet radiation have equivalent flux and brightness. In fact, the physical process of ER emission is not different from that of radiation emission from a single bend. However, radiation from the setup in Fig. 1(a) exhibits special features, due to a narrower opening angle of ER over SR from bends. Although for many experiments using infrared radiation one can accept large collection angles in the horizontal and vertical directions, as the wavelength gets longer ER can be advantageous in terms of simplicity of the photon beamline [15] e.g. in infrared microspectroscopy applications.

ER theory is a part of the more general SR theory, very much like Undulator Radiation (UR) theory is a part of SR theory. Similarly to the UR case, also for ER the knowledge of the applicability region of the far-field formulas and corrections for near-field effects are of practical importance. In most practical cases, the distance between ER source and observer (i.e. the first optical element of the photon beamline) are comparable or even much smaller than the length of the straight section, which plays the role of the length of the insertion device for ER.

In this paper we developed a theory of near-field ER based on Fourier Optics (FO) techniques. These techniques can be exploited without limitations for ER setups, because the paraxial approximation can always be applied in the case of electrons in ultra-relativistic motion [16]. The use of the paraxial approximation allows reconstruction of the field in the near-zone from the knowledge of the far-field data. The solvability of the inverse problem for the field allows characterization of any ER setup, starting from the far-zone field,

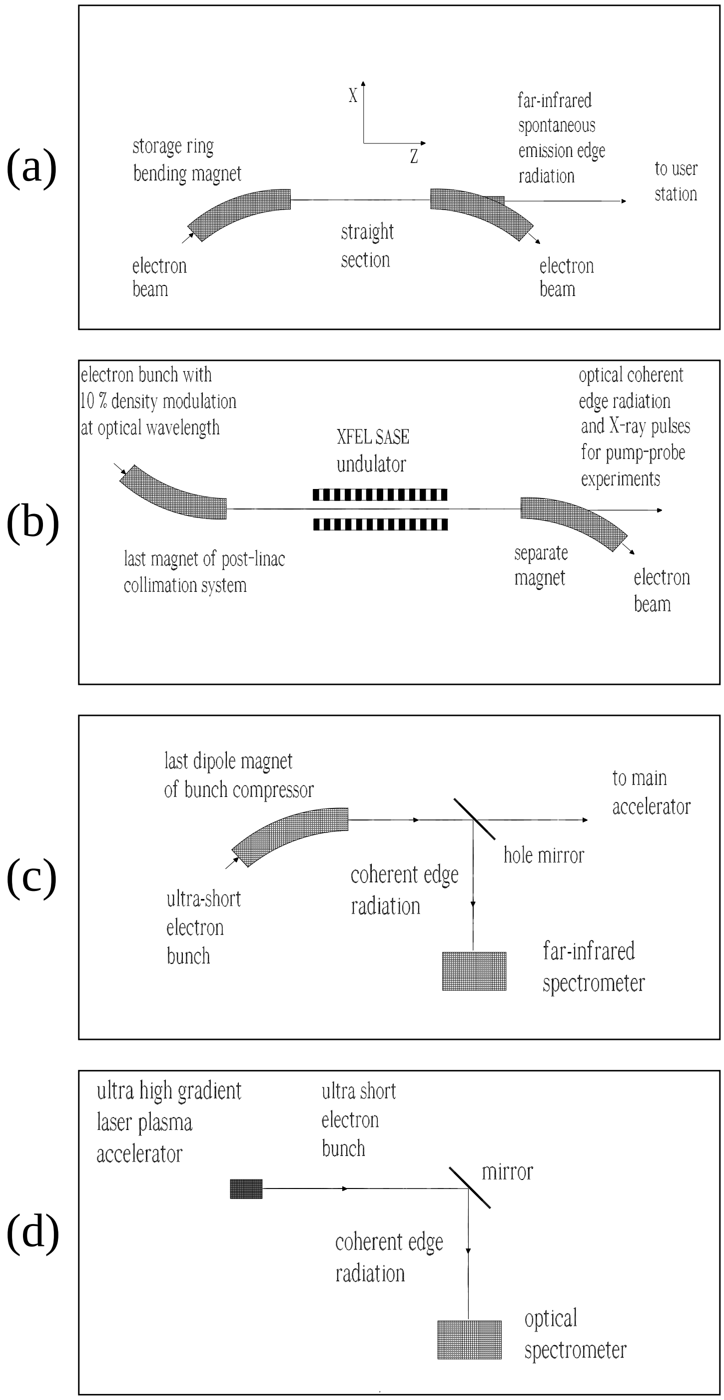

Fig. 1. Four main types of edge radiation setups: (a) Far-infrared beamline for synchrotron radiation source using edge radiation. (b) Arrival-time monitor for XFEL source using optical coherent edge radiation. (c) Electron bunch length monitor for XFEL using far-infrared coherent edge radiation. (d) Ultra-short electron bunch diagnostic for laser-plasma accelerator facility using optical coherent edge radiation.

in terms of virtual sources. These sources exhibit a plane wavefront, and can be pictured as waists of laser-like beams. Using this kind of description we develop our theory in close relation with laser-beam optics. In particular, usual FO can be exploited to characterize the field at any distance, providing a tool for designing and analyzing ER setups.

It is the purpose of this article to discuss the principles of production and properties for all applications of ER. First, we treat the relatively simple case of ER from a setup composed by straight section and two bending magnets at its ends (see Fig. 1(a)). We begin calculating an analytical expression for ER from a single electron in the far-zone. Then, we characterize the near-zone with the help of the virtual-source technique. Two alternative techniques for the field propagation are given, based on a single virtual source located in the middle of the ER setup, and based on two virtual sources located at its edges.

Based on this study-case we turn to analyze a more complicated setup, consisting of an undulator preceded and followed by two straight sections and two bends (see Fig. 1(b)). ER from this kind of setup is commonly known as Transition Undulator Radiation (TUR). The first study on TUR appeared more than a decade ago in [17]. In that work it was pointed out for the first time that, since an electron entering or leaving an undulator experiences a sudden change in longitudinal velocity, highly collimated radiation with broadband spectrum, similar to transition radiation, had to be expected in the low-frequency region in addition to the usual UR. Reference [17] constitutes a theoretical basis for many other studies. Here we remind only a few [9, 18, 19, 20, 21], dealing both with theoretical and experimental issues. More recently, TUR has been given consideration in the framework of X-ray Free-Electron Laser (XFEL) projects like [22, 23, 24]. For example, an arrival-time monitor for XFELs using infrared coherent ER from a setup similar to that in Fig. 1(b) has been proposed in [25], which should be used for pump-probe experiments with femtosecond-scale resolution. In view of these applications, there is a need to extend the characterization of TUR to the near-zone, and to the coherent case. From this viewpoint, specification of what precedes and follows the undulator is of fundamental importance. As has been recognized for TUR many years ago [9], if this information is not known, any discussion about the intensity distribution of TUR is meaningless. According to our approach, the two straight sections and the undulator in the setup in Fig. 1(b) will be associated to virtual sources with plane wavefronts. The field from the setup can then be described, in the near as well as in the far-zone, as a superposition of laser-like beams, radiating at the same wavelength and separated by different phase shifts.

Our study makes consistent use of both dimensional analysis and comparisons with outcomes from numerical simulation. All simulations in this paper are performed with the help of the computer code SRW [26].

2 General relations for edge radiation phenomena

2.1 Physical discussion of some numerical experiment

This Section constitutes an attempt to introduce ER theory to readers in as intuitive and simple a fashion as possible by simulating the spectral energy density per unit angle as a function of observation angles for the geometry in 1(a). For this purpose we take advantage of the code SRW [26], which provides a numerical solution of Maxwell's equations.

The origin of a Cartesian coordinate system is placed at the center of straight section. The z-axis is in the direction of straight section and electron motion is in xz plane. Parameters of the problem are the radiation wavelength λ, the radius of the bend R, the relativistic Lorentz factor γ, the length of the straight section L and, additionally, the position of the observation plane down the beamline, z. We work in the far zone. In this Section it is operatively defined as a region where z is large enough, so that the simulated spectral energy density per unit angle does not show dependence on z anymore.

ER carries advantages over bending magnet radiation in the limit for $\lambdabar/\lambdabar_c \gg 1$, where $\lambdabar_c \sim R/\gamma^3$ (here $\lambdabar = \lambda/(2\pi)$ is the reduced wavelength) is the critical wavelength of bending magnet radiation. We will work, therefore, in this limit. We set $\gamma = 3.42 \cdot 10^4$ (17.5 GeV), $R = 400$ m, which are typical values for XFELs. Note that in this case $\lambda_c \simeq 0.1$Å. Here we take $\lambda = 400$ nm. We begin with the case $L = 0$ (bending magnet), and we increase the straight section length (see Fig. 2). As one can see from the figure, radiation becomes more collimated, up to about $L \simeq \gamma^2\lambdabar \simeq 100$ m (case (d)), where the collimation angle reaches $1/\gamma \sim 30\mu$rad. Further increase of L only leads to the appearance of finer structures in the radiation profile. It is important to remark that the total number of photons in the ± 1 mrad window shown in Fig. 2(a) is roughly the same in the $\pm 100\mu$rad window in Fig. 2(d). It is clear that the length of the straight section L is strongly related with the collimation of the radiation.

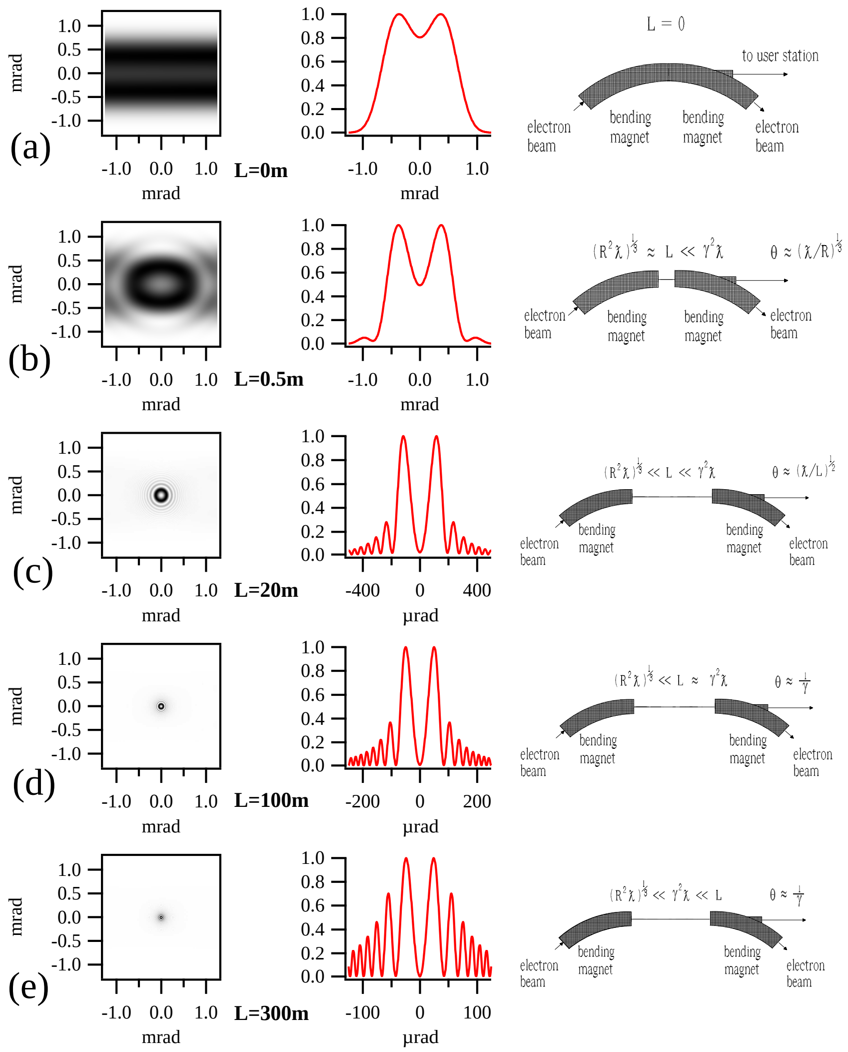

Fig. 2. Illustrative calculations of the effect of bending magnet separation on the directivity diagram of the radiation. The bending magnet radius $R = 400$ m, the relativistic factor $\gamma = 3.42 \cdot 10^4$, and the wavelength of interested $\lambda = 400$ nm are fixed, while the straight section length varies from $L = 0$ up to $L \gg \gamma^2 \lambdabar \simeq 100$ m. In this setup (as well as in all others in this paper) $\lambda \gg \lambda_c \simeq 0.1$Å. Case (a) is a bending magnet setup. Case (b) is a complex setup, where the radiation beam divergence is practically the same as in (a). Case (c) illustrates an ER setup. Bending magnet separation dramatically lowers the radiation beam divergence. (d) Optimal bending magnet separation. The straight section length $L \simeq \gamma^2 \lambdabar$ corresponds to a radiation beam divergence $\theta \simeq 1/\gamma$. (e) Further increase of L only leads to the appearance of finer structures in the radiation profile. 2D plots on the left show the spectral energy density per unit angle as a function of the horizontal and vertical angles θ_x and θ_y for various lengths of the straight section. Middle plots are obtained cutting the 2D angular distributions at $x = 0$. Right plots show a schematic of the considered layout.

2.2 Similarity techniques

To study ER further we apply similarity techniques. Similarity is a special symmetry where a change in scale of independent variables can be compensated by a similarity transformation of other variables. This is a familiar concept in hydrodynamics, where the cardinal example is given by the Reynolds number. Similarity allows one to reduce the number of parameters to a few dimensionless ones that are directly linked to the physics of the process, and that control it in full. Such parameters are found by analysis of the underlying equations characterizing the system under study. In this Section we limit ourselves to list them, to show their correctness with the help of the code SRW, and to describe their physical meaning. This allows one to obtain general properties of the ER process. A comprehensive theory of ER will be presented in the following Sections.

For the setup in Fig. 1(a), two dimensionless parameters controlling the radiation characteristics can be extracted from Maxwell's equations. In the next Section we will show how these parameters can be derived. Here we limit ourselves to write them:

$$\delta \equiv \frac{\sqrt[3]{R^2 \lambdabar}}{L} , \quad \phi \equiv \frac{L}{\gamma^2 \lambdabar} . \qquad (1)$$

The detector is supposed to be far away from the source so that the above-given definition of far-zone holds.

The most important general statement concerning ER is that all possible situations correspond to different values of the two dimensionless parameters δ and ϕ.

Note that the working limit $\bar{\lambda}/\bar{\lambda}_c \gg 1$ means $\phi \cdot \delta \ll 1$ in terms of dimensionless parameters. For any two cases characterized by the same values of δ and ϕ, the spectral energy density per unit angle from the setup in Fig. 1(a) will "look" the same in terms of angles scaled to $\sqrt{\bar{\lambda}/L}$, i.e. $\hat{\theta} = \theta/\sqrt{\bar{\lambda}/L}$. In other words, data for different sets of problem parameters corresponding to the same values of δ and ϕ reduce to a single curve when properly normalized. We tested the scaling properties of ER by running numerical simulations with the first principle computer code SRW. We used two different sets of dimensional parameters corresponding to the same case in terms of parameters δ and ϕ, and we checked that the spectral energy density per unit angle normalized to their maximal values are identical. Results are presented in Fig. 3 and Fig. 4, where the normalized spectral energy density per unit angle is indicated with $I/I_{\max}$.

When $\delta \sim 1$, the presence of the bending magnet radiation strongly influences the radiation profile (see Fig. 3(a)). When δ decreases up to $\delta \ll 1$, one can neglect bending magnet contributions (see Fig. 3(b)): what is left in this case is ER. These situations are realized, for example, if one works at fixed $\bar{\lambda}$, γ and R while increasing the length L as in the case of Fig. 2. It follows that δ is responsible for the relative weight of ER and bending magnet radiation contributions in the radiation profile. Since we are interested in ER emission, it is natural to consider more in detail the limit for $\delta \ll 1$. In this case, results are independent on the actual value of δ, and the only parameter left is ϕ. This fact can be seen from Fig. 3(b), where the two sets of dimensional parameters refer to two different value of $\delta \ll 1$. We will name this situation the sharp-edge asymptote.

In the limit for $\phi \ll 1$, the opening angle of the radiation is independent of

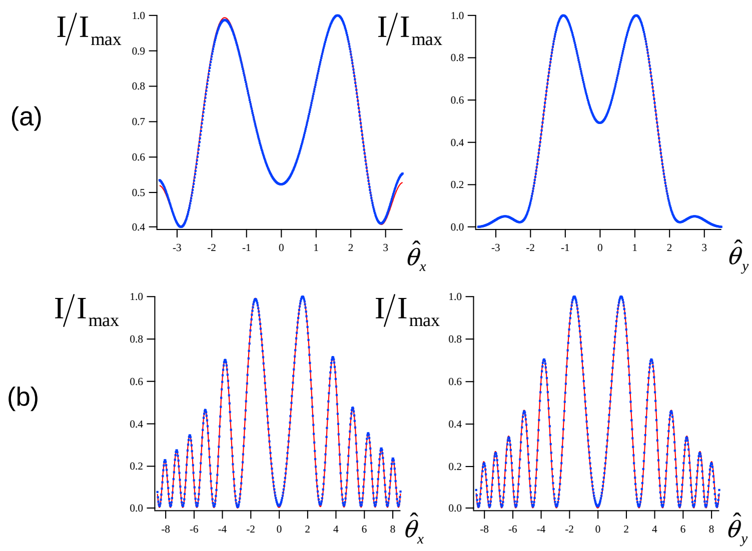

Fig. 3. Verification of similarity techniques. Left and right plots show the normalized spectral energy density per unit angle as a function of the horizontal and vertical angles $\hat{\theta}_x$ and $\hat{\theta}_y$ respectively (at $\hat{\theta}_y = 0$ and $\hat{\theta}_x = 0$ respectively). (a) Case $\delta \simeq 0.43$ and $\phi \simeq 6.7 \cdot 10^{-3}$. The solid curve is the result of SRW calculations with $L = 0.5$ m, $R = 400$ m, $\lambda = 400$ nm at 17.5 GeV. The dotted curve is the result for $L = 1$ m, $R = 800$ m, $\lambda = 800$ nm at 17.5 GeV. (b) Case $\delta \ll 1$ and $\phi \simeq 4$. The solid curve is the result of SRW calculations with $L = 300$ m, $R = 400$ m, $\lambda = 400$ nm, at 17.5 GeV (corresponding to $\delta \simeq 7 \cdot 10^{-4}$). The dotted curve is the result for $L = 150$ m, $R = 400$ m, $\lambda = 800$ nm at 8.5 GeV (corresponding to $\delta \simeq 2 \cdot 10^{-3}$).

the actual value of ϕ too. In this case we obtain the universal plot shown in Fig. 4, and one talks about a self-similar behavior of the profile of the spectral energy density per unit angle, which asymptotically approaches the self-similar form $I/I_{\max} = F(\hat{\theta}_x, \hat{\theta}_y)$. Note that the separation distance L between the bends dramatically lowers the radiation beam divergence, but the characteristic angle of emission is still larger than $1/\gamma$. In fact, radiation peaks at $\theta \simeq 2.2\sqrt{\lambda\!\!\!^{-}/L}$. When ϕ increases, radiation becomes better and better collimated, up to angles $\theta \sim 1/\gamma$. This happens for values $\phi \simeq 1$. Radiation has reached the best possible collimation angle and further increase of ϕ

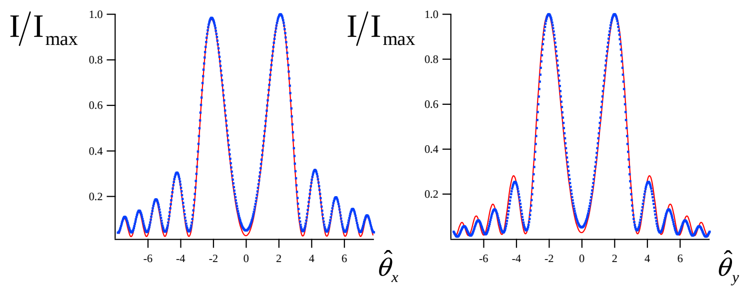

Fig. 4. Illustration of self-similarity techniques. Left and right plots show the normalized spectral energy density per unit angle as a function of the horizontal and vertical angles $\hat{\theta}_x$ and $\hat{\theta}_y$ respectively (at $\hat{\theta}_y = 0$ and $\hat{\theta}_x = 0$ respectively). The profile of the spectral energy density per unit angle asymptotically approaches the self-similar form $I/I_{\mathrm{max}} = F(\hat{\theta}_x, \hat{\theta}_y)$ for $\delta \ll 1$ and $\phi \ll 1$. The solid curve is the result of SRW calculations with $\delta \simeq 0.02$ and $\phi \simeq 0.13$. The dotted curve refers to the case $\delta = 0.01$ and $\phi = 0.27$ instead.

(see Fig. 3(b)) only modifies fine structures in the radiation profile.

2.3 Qualitative description

It is possible to present intuitive arguments to explain why all problem parameters (R, γ, L and $\lambdabar$) are effectively grouped in δ and ϕ.

To this purpose let us consider first the parameter δ. By definition, $1/\delta$ is a measure of the straight section length L in units of a characteristic length $\sqrt[3]{R^2\lambdabar}$.

To explain the meaning of the quantity $\sqrt[3]{R^2\lambdabar}$, following [27] we consider Fig. 5(a), and we focus on the region of parameters $\lambdabar \ll R$ and $\gamma^2 \gg 1$. A posteriori, this region of parameters will turn out to correspond to an angular dimension along the trajectory $2\theta \ll 1$ within the bending magnet. Radiation from an electron passing through the setup is observed through

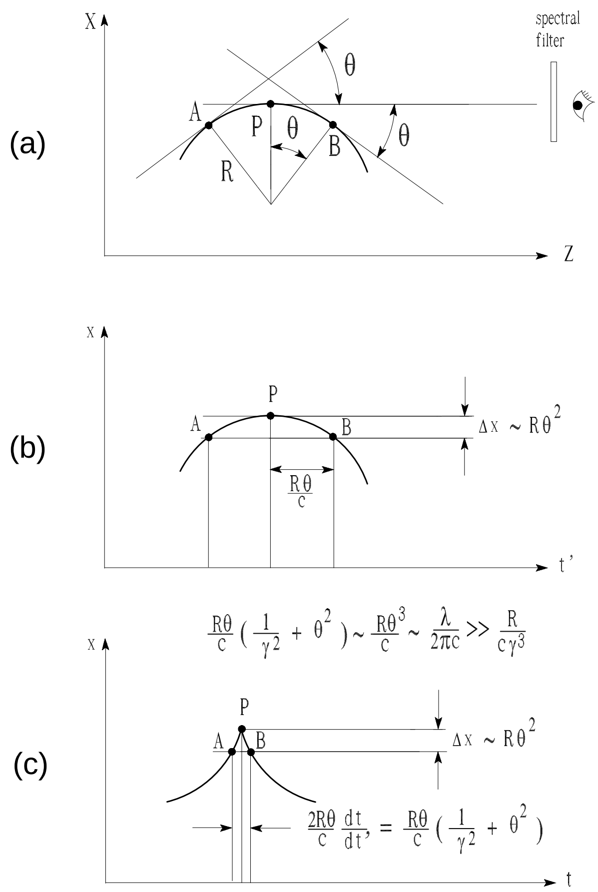

Fig. 5. Geometry for SR from a bending magnet.

a spectral filter by a fixed observer positioned on the tangent to the bend at point P. Electromagnetic sources propagate through the system, as a function of time, as shown in Fig. 5(b). However, electromagnetic signals emitted at time t' at a given position $x(t')$ arrive at the observer position at a different time t, due to the finite speed of light. As a result, the observer in Fig. 5(a) sees the electromagnetic source motion as a function of t. What one needs to know, in order to calculate the electric field, is the apparent motion $x(t)$ shown in Fig. 5(c), which is a hypocycloid, and not the real motion $x(t')$. In fact, the electric field at the observation point is proportional to the second derivative of the x-coordinate with respect to the retarded time t, because the observer sees everything as delayed. We discuss the case when the source is heading towards the observer. Using the fact that $\theta \ll 1$, one obtains the well-known relation $dt/dt' = 1/2 \cdot (1/\gamma^2 + \theta^2)$. The observer sees a time-compressed motion of the sources, which go from point A to point B in an apparent time corresponding to an apparent distance $2R\theta dt/(dt')$. Let us assume (this assumption will be justified in a moment) $\theta^2 > 1/\gamma^2$. In this case one has $2R\theta dt/(dt') \simeq R\theta^3$. Obviously one can distinguish between radiation emitted at point A and radiation emitted at point B only when $R\theta^3 \gg \lambda\!\!\!^{-}$, i.e. for $\theta \gg (\lambda\!\!\!^{-}/R)^{1/3}$. This means that, as concerns the radiative process, we cannot distinguish between point A and B on the bend such that $R\theta \lesssim (R^2\lambda\!\!\!^{-})^{1/3}$. It does not make sense at all to talk about the position where electromagnetic signals are emitted within $L_{fb} = (R^2\lambda\!\!\!^{-})^{1/3}$ (here we are assuming that the bend is longer than L_{fb}). This characteristic length is called the formation length for the bend. The formation length can also be considered as a longitudinal size of a single-electron source. Note that a single electron always produces diffraction-limited radiation $d \cdot \Delta\theta \sim \lambda\!\!\!^{-}$, d being the transverse size and $\Delta\theta$ the divergence of the source. Since $d \sim L_{fb}\Delta\theta$, it follows that the divergence angle $\Delta\theta$ is strictly related to L_{fb} and $\lambda\!\!\!^{-}$: $\theta \sim \sqrt{\lambda\!\!\!^{-}/L_{fb}}$. One may check that, using $L_{fb} \sim \sqrt[3]{R^2\lambda\!\!\!^{-}_c}$, one obtains $\theta \sim \sqrt[3]{\lambda\!\!\!^{-}/R}$; in particular, at $\lambda\!\!\!^{-} \sim \lambda\!\!\!^{-}_c \sim R/\gamma^3$ one obtains $\theta \sim 1/\gamma$, as is well-known for bending magnet radiation.

Let us now consider the case of a straight section of length L inserted between the two halves of a bend. Since we cannot distinguish between points within L_{fb}, the case $L = 0$ is obviously indistinguishable from the case $L \ll L_{fb}$. Significant deviations from the bending magnet case are to be expected when $L \gtrsim L_{fb}$, i.e. when $\delta \lesssim 1$. This hints to the fact that δ is responsible for the relative weight of ER and bending magnet radiation contributions in the radiation profile.

Let us now discuss the parameter ϕ. By definition, ϕ is a measure of the straight section length L in units of a characteristic length $\gamma^2 \lambda\!\!\!^{-}$. One can still use the same reasoning considered for the bend to define a region of the trajectory where it does not make sense to distinguish between different points. In the case of a straight section of length L connecting A and B, $dt/dt' = 1/(2\gamma^2)$. It follows that the apparent distance AB is equal to $L/(2\gamma^2)$. Since it does not make sense to distinguish between points within the apparent electron trajectory such that $L/(2\gamma^2) \lesssim \lambda\!\!\!^{-}$, one obtains a critical length of interest $\sim \gamma^2 \lambda\!\!\!^{-}$. This hints to the fact that for values $\phi \simeq 1$ radiation has reached the best collimation angle.

Note that for ultrarelativistic systems in general, the formation length is always much longer than the radiation wavelength. This is related with a large compression factor dt/dt'. For comparison, in the case of non-relativistic motion the compression factor $dt/dt' \simeq 1$, and the formation length is simply of order of the radiation wavelength. The counterintuitive result follows, that for ultrarelativistic systems one cannot localize sources of radiation within a macroscopic part of the trajectory.

3 Paraxial approximation

In the next two Sections we present a complete theory of ER. All electrodynamical theories are based on the presence of small or large parameters.

In general, the theory of Synchrotron Radiation (SR) is based on the exploitation, for ultra-relativistic particles, of the small parameter γ^{-2}. By this, Maxwell's equations are reduced to much simpler equations with the help of paraxial approximation. ER theory constitutes a particular case of SR theory, based on the extra small-parameter δ.

Here and everywhere else in this paper we will make consistent use of Gaussian units.

In this Section we deal with the paraxial approximation of Maxwell's equations. We will treat both near and far zone cases, with special attention to the applicability region of equations describing ER in different regions of the parameter space.

Whatever the method used to present results, one needs to solve Maxwell's equations in unbounded space. We introduce a cartesian coordinate system, where a point in space is identified by a longitudinal coordinate z and transverse position $\vec{r}$. Accounting for electromagnetic sources, i.e. in a region of space where current and charge densities are present, the following equation for the field in the space-frequency domain holds in all generality:

$$c^2\nabla^2\vec{\bar{E}} + \omega^2\vec{\bar{E}} = 4\pi c^2\vec{\nabla}\bar{\rho} - 4\pi i\omega\vec{\bar{j}}\,, \tag{2}$$

where $\bar{\rho}(z,\vec{r},\omega)$ and $\vec{\bar{j}}(z,\vec{r},\omega)$ are the Fourier transforms [2] of the charge density $\rho(z,\vec{r},t)$ and of the current density $\vec{j}(z,\vec{r},t)$. Eq. (2) is the well-known

[2] We explicitly write the definitions of the Fourier transform and inverse transform of a function $f(t)$ in agreement with the notations used in this paper. The Fourier transform and inverse transform pair reads:

$$\bar{f}(\omega) = \int \mathrm{d}t\, f(t) \exp\left[i\omega t\right] \ ; \ \ f(t) = \frac{1}{2\pi}\int \mathrm{d}\omega\, \bar{f}(\omega) \exp\left[-i\omega t\right] .$$

Helmholtz equation. Here $\vec{\bar{E}}$ indicates the Fourier transform of the electric field in the space-time domain.

A system of electromagnetic sources in the space-time can be conveniently described by $\rho(z, \vec{r}, t)$ and $\vec{j}(z, \vec{r}, t)$. Considering a single electron and using the Dirac delta distribution, we can write

$$\rho\,(z, \vec{r}, t) = -e\delta\,(\vec{r} - \vec{r}_0(t))\,\delta(z - z_0(t)) = -\frac{e}{v_z(z)}\delta\,(\vec{r} - \vec{r}_0(z))\,\delta\left(\frac{s(z)}{v} - t\right) \tag{3}$$

$$\vec{j}\,(z, \vec{r}, t) = \vec{v}(t)\rho\,(z, \vec{r}, t)\ , \tag{4}$$

where $(z_0(t), \vec{r}_0(t))$ and $\vec{v}(t)$ are, respectively, position and velocity of the particle at a given time t in a fixed reference frame, v_z is the longitudinal velocity of the electron , and $(-e)$ is the electron charge. Additionally, we defined the curvilinear abscissa $s(z) = vt(z)$, where $v = \left|\vec{v}(t(z))\right|$ is a constant. In the space-frequency domain the electromagnetic sources transform to:

$$\bar{\rho}(\vec{r}, z, \omega) = -\frac{e}{v_z(z)}\delta\,(\vec{r} - \vec{r}_0(z))\exp\left[\frac{i\omega s(z)}{v}\right] \tag{5}$$

and

$$\vec{\bar{j}}(\vec{r}, z, \omega) = \vec{v}(z)\bar{\rho}(\vec{r}, z, \omega) \tag{6}$$

Since we will only be interested in the transverse components of the field, from now on we will consider the transverse field envelope $\vec{\tilde{\bar{E}}}$, a 2D vector defined in the space-frequency domain as $\vec{\tilde{\bar{E}}} = \vec{\bar{E}}_\perp \exp[-i\omega z/c]$, the symbol "$\perp$" indicating projection on the transverse plane. By substitution in Helmholtz equation we obtain

$$\left(\nabla^2 + \frac{2i\omega}{c}\frac{\partial}{\partial z}\right)\vec{\tilde{E}} = \frac{4\pi e}{v_z(z)} \exp\left[i\omega\left(\frac{s(z)}{v} - \frac{z}{c}\right)\right]\left[\frac{i\omega}{c^2}\vec{v}_\perp(z) - \vec{\nabla}_\perp\right]\delta\left(\vec{r} - \vec{r}_0(z)\right), \quad (7)$$

where, according to our notation, $\vec{\nabla}_\perp$ indicates a gradient with respect to transverse coordinates only, and $\vec{v}_\perp$ is the transverse velocity of the electron. Eq. (7) is still fully general and may be solved in any fixed reference system (x, y, z) of choice with the help of an appropriate Green's function.

When the longitudinal velocity of the electron, v_z, is close to the speed of light c, one has $\gamma_z^2 \gg 1$, where $\gamma_z^{-2} = 1 - v_z^2/c^2$. The Fourier components of the source are then almost synchronized with the electromagnetic wave travelling at the speed of light. Note that this synchronization is the reason for the time compression factor described in Section 2.3. In this case, the phase $\omega(s(z)/v - z/c)$ is a slow function of z compared to the wavelength. For example, in the particular case of motion on a straight section, one has $s(z) = z/v_z$, so that $\omega(s(z)/v - z/c) = \omega z/(2\gamma_z^2 c)$, and if $\gamma_z^2 \gg 1$ such phase grows slowly in z with respect to the wavelength. For a more generic motion, one similarly obtains:

$$\omega\left(\frac{s(z_2) - s(z_1)}{v} - \frac{z_2 - z_1}{c}\right) = \int_{z_1}^{z_2} d\bar{z}\frac{\omega}{2\gamma_z^2(\bar{z})c}, \quad (8)$$

Mathematically, the phase in Eq. (8) enters in the Green's function solution of Eq. (7) as a factor in the integrand. As we integrate along z, the factor $\omega(s(z)/v - z/c)$ leads to an oscillatory behavior of the integrand over a certain integration range in z. Such range can be identified with the value of $z_2 - z_1$ for which the right hand side of Eq. (8) is of order unity, and it is naturally defined as the radiation formation length L_f of the system at frequency ω. Of course there exist some freedom in the choice of such definition: "order of unity" is not a precise number, and reflects the fact that there is no abrupt threshold between "oscillatory" and "non-oscillatory" behavior of the integrand in the solution of Eq. (7). It is easy to see by inspection of Eq. (8) that if v_z is sensibly smaller than c, but still of order c, i.e. $v_z \sim c$ but $1/\gamma_z^2 \sim 1$, then $L_f \sim \lambdabar$. On the contrary, when v_z is very close to c, i.e. $1/\gamma_z^2 \ll 1$, the right hand side of Eq. (8) is of order unity for $L_f = z_2 - z_1 \gg \lambdabar$. When the radiation formation length is much longer than $\lambdabar$, $\vec{\widetilde{E}}$ does not vary much along z on the scale of $\lambdabar$, that is $\mid \partial_z \widetilde{E}_{x,y} \mid \ll \omega/c \mid \widetilde{E}_{x,y} \mid$. Therefore, the second order derivative with respect to z in the ∇^2 operator on the left hand side of Eq. (7) is negligible with respect to the first order derivative, and Eq. (7) can be simplified to

$$\left({\nabla_\perp}^2 + \frac{2i\omega}{c}\frac{\partial}{\partial z}\right)\vec{\widetilde{E}} = \frac{4\pi e}{c}\exp\left[i\omega\left(\frac{s(z)}{v} - \frac{z}{c}\right)\right]\left[\frac{i\omega}{c^2}\vec{v}_\perp(z) - \vec{\nabla}_\perp\right]\delta\left(\vec{r} - \vec{r}_0(z)\right) , \tag{9}$$

where, as said before, we consider transverse components of $\vec{\widetilde{E}}$, and we substituted $v_z(z)$ with c, based on the fact that $1/\gamma_z^2 \ll 1$. Eq. (9) is Maxwell's equation in paraxial approximation. Eq. (7), which is an elliptic partial differential equation, has thus been transformed into Eq. (9), that is of parabolic type. Note that the applicability of the paraxial approximation depends on the ultra-relativistic assumption $\gamma^2 \gg 1$ but not on the choice of the z axis. If, for a certain choice of the longitudinal z direction, part of the trajectory is such that $\gamma_z^2 \sim 1$, the formation length is very short ($L_f \sim \lambdabar$), and the radiated field is practically zero. As a result, Eq. (9) can always be applied, i.e. the paraxial approximation can always be applied, whenever $\gamma^2 \gg 1$.

Complementarily, it should also be remarked here that the status of the paraxial equation Eq. (9) in Synchrotron Radiation theory is different from that of the paraxial equation in Physical Optics. In the latter case, the paraxial approximation is satisfied only by small observation angles. For example, one may think of a setup where a thermal source is studied by an observer positioned at a long distance from the source and behind a limiting aperture. Only if a small-angle acceptance is considered the paraxial approximation can be applied. On the contrary, due to the ultra-relativistic nature of the emitting electrons, contributions to the SR field from parts of the trajectory with formation length $L_f \gg \lambdabar$ (the only non-negligible) are highly collimated. As a result, the paraxial equation can be applied at any angle of interest, because it practically returns zero field at angles where it should not be applied.

Finally, since the characteristic scale of variation of $\vec{\widetilde{E}}$ is much larger than $\lambdabar$, the paraxial approximation is valid up to distances of the observer from the electromagnetic sources of order $\lambdabar$.

The Green's function for Eq. (9), namely the solution corresponding to the unit point source can explicitly be written in an unbounded region as

$$G(\vec{r} - \vec{r'}, z - z') = -\frac{1}{4\pi|z - z'|} \exp\left[i\omega \frac{|\ \vec{r} - \vec{r'}\ |^2}{2c|z - z'|}\right] , \tag{10}$$

Note that when $z - z' < 0$ the paraxial approximation does not hold, and the paraxial wave equation Eq. (9) should be substituted, in the space-frequency domain, by the more general Helmholtz equation. However, the radiation formation length for $z - z' < 0$ is very short with respect to the case $z - z' > 0$, i.e. there is effectively no radiation for observer positions $z - z' < 0$. As a result, in this paper we will consider only $z - z' > 0$. The reason why $|z - z'|$ is present in Eq. (10) (while $z - z' > 0$ always) is that, mathematically, the Green's function G is actually related to the *operator* on the left hand side of Eq. (9), and not to the whole equation. For example, when dealing with wavefront propagation, one must consider the homogeneous version of Eq. (9), and the same Green's function in Eq. (10) can be used, as we will see, to propagate the electric field. In this case, propagation can be performed in the backward direction as well, i.e. for $z - z' < 0$.

Note that Eq. (10) automatically include information about the boundary condition for the field. In the present case, since we are dealing with unbounded space, the field vanishes at large distance from the sources. Due to this fact, the Green's function in Eq. (10) is a scalar function, while in general it admits tensorial values. Using the definition of Green's function, and carrying out integration over transverse coordinates we obtain

$$\vec{\bar{E}} = \frac{4\pi e}{c} \int_{-\infty}^{z} dz' \left\{ \frac{i\omega}{c^2} \vec{v}_\perp(z') G\left(\vec{r} - \vec{r}_0(z'), z - z'\right) + \left[\vec{\nabla}'_\perp G\left(\vec{r} - \vec{r'}, z - z'\right)\right]_{\vec{r'} = \vec{r}_0(z')} \right\}$$
$$\times \exp\left[i\omega \left(\frac{s(z)}{v} - \frac{z}{c} \right) \right] , \qquad (11)$$

where $\vec{\nabla}'_\perp$ indicates derivatives with respect to $\vec{r'}$. Explicit substitution of Eq. (10) yields the following result

$$\vec{\bar{E}}(z, \vec{r}) = -\frac{i\omega e}{c^2} \int_{-\infty}^{z} dz' \frac{1}{z - z'} \left[\frac{\vec{v}_\perp(z')}{c} - \frac{\vec{r} - \vec{r}_0(z')}{z - z'} \right]$$
$$\times \exp\left\{ i\omega \left[\frac{\mid \vec{r} - r_0(\vec{z'}) \mid^2}{2c(z - z')} + \int_0^{z'} d\bar{z} \frac{1}{2\gamma_z^2(\bar{z}) c} \right] \right\} , \qquad (12)$$

where we the choice of integration limits in $d\bar{z}$ indicates that the electron arrives at position $z = 0$ at time $t_a = 0$. Eq. (12) is valid at any observation position z such that the paraxial approximation is valid, i.e. up to distances between the observer and the electromagnetic sources comparable with the radiation wavelength. One may recognize two terms in Eq. (12). The first in $\vec{v}_{\perp}(z')$ can be traced back to the current term on the right hand side of Eq. (7), while the second, in $\vec{r} - \vec{r}_0(z')$, corresponds to the gradient term on the right hand side of Eq. (7).

Eq. (12) is used as starting point for numerical codes like SRW. The only approximation used is the paraxial approximation. This rules out the possibility of using SRW to study the region of applicability of the paraxial approximation. However, once the paraxial approximation is granted for valid, SRW, or Eq. (12), can be used to investigate the applicability of ER theory, which is built within the constraints of the paraxial approximation. Note that the evaluation of the field begins with the knowledge of the trajectory followed by the electron, which is completely generic. In other words, one needs to know the electromagnetic sources to evaluate the field at any position z down the beamline.

Alternatively, the knowledge of the far-zone field distribution, i.e. a limit of Eq. (12), allows one to specify an algorithm to reconstruct the field in the near zone up to distances of the observer from the sources much larger than $\lambda\!\!\!^{-}$. An important characteristic of this algorithm is that it works within the region of applicability of the paraxial approximation, $\gamma^2 \gg 1$ only. Such algorithm was developed in [16] to deal with SR problems in full generality, and will be used in this paper to develop our ER theory. It follows three major steps.

I. The first step is the characterization of ER emission in the far zone. From Eq. (12) follows directly:

$$\vec{\widetilde{E}}(z, \vec{\theta}) = -\frac{i\omega e}{c^2 z} \int\limits_{-\infty}^{z} dz' \left(\frac{\vec{v}_\perp(z')}{c} - \vec{\theta}\right) \times \exp\left[i\omega \int\limits_{0}^{z'} \frac{d\bar{z}}{2c\gamma_z^2(\bar{z})} + \frac{i\omega}{2c}\left(z\,\theta^2 - 2\vec{\theta}\cdot\vec{r}_0(z') + z'\theta^2\right)\right], \tag{13}$$

where $\vec{\theta} = \vec{r}/z$ defines the observation direction, and $\theta \equiv |\vec{\theta}|$. Note that the concept of formation length is strictly related to the concept of observation angle of interest. In fact, given a certain formation length L_f, and substituting it into the phase in $z'\theta^2$ in Eq. (13), one sees that the integrand starts to be highly oscillatory for angles $\theta \simeq \sqrt{\lambda\!\!\!^{-}/L_f}$. Eq. (13) is taken as the starting point for our algorithm.

II. The second step consists in interpreting the far-zone field in Eq. (13) as a laser-like beam, generated by one or more virtual sources. These sources are not present in reality, because they are located at positions inside the magnetic setup, but they produce the same field as that of the real system. Hence the denomination "virtual". A virtual source is similar, in many aspects, to the waist of a laser beam and, in our case, exhibits a plane wavefront. It is then completely specified, for any given polarization component, by a real-valued amplitude distribution of the field, located at a fixed longitudinal position.

Suppose we know the field at a given plane at z, and we want to calculate the field at another plane at z_s. In paraxial approximation and in free space, the homogeneous version of Eq. (9) holds for the complex envelope $\vec{\widetilde{E}}$ of the Fourier transform of the electric field along a fixed polarization component, that is $[{\nabla_\perp}^2 + (2i\omega/c)\partial_z]\vec{\widetilde{E}} = 0$. One has to solve this equation with a given initial condition at z, which defines a Cauchy problem. We obtain

$$\vec{\widetilde{E}}(z_s,\vec{r}) = -\frac{2i\omega}{c}\int d\vec{r'}\,\vec{\widetilde{E}}(z,\vec{r'})G\left(\vec{r}-\vec{r'},z_s-z\right)~, \tag{14}$$

where the integral is performed over the transverse plane and the Green's function G in unbounded space is given in Eq. (10). Similarly as before, it is important to remark that since $\vec{\widetilde{E}}$ is a slowly-varying function with respect to the wavelength, one cannot resolve the evolution of the field on a longitudinal scale of order of the wavelength within the accuracy of the paraxial approximation. In order to do so, the paraxial equation should be replaced by the more general Helmholtz equation. Let us now consider the limit $z \longrightarrow \infty$, with finite ratio $\vec{r'}/z$. In this case, the exponential function in Eq. (14) can be expanded giving

$$\vec{\widetilde{E}}(z_s,\vec{r}) = \frac{i\omega}{2\pi c z}\int d\vec{r'}\,\vec{\widetilde{E}}(z,\vec{r'})\exp\left[-\frac{i\omega}{2cz}\left(r^2-2\vec{r}\cdot\vec{r'}+\frac{z_s r^2}{z}\right)\right]. \tag{15}$$

Letting $\vec{\theta} = \vec{r'}/z$ we have

$$\vec{\widetilde{E}}\left(z_s,\vec{r}\right) = \frac{i\omega z}{2\pi c}\int d\vec{\theta}\exp\left[-\frac{i\omega\theta^2}{2c}(z+z_s)\right]\vec{\widetilde{E}}\left(z,\vec{\theta}\right)\exp\left[\frac{i\omega}{c}\vec{r}\cdot\vec{\theta}\right]~, \tag{16}$$

where the transverse vector $\vec{r}$ defines a transverse position on the virtual source plane at $z = z_s$. Eq. (16) allows to calculate the field at the virtual source once the field in the far zone is known. The specification of the virtual source amounts to the specification of an initial condition for the electric field, that is then propagated at any distance. From this viewpoint, identification of the position $z = z_s$ with the virtual source position is possible independently of the choice of z_s. In other words, like in laser physics, the SR field can be propagated starting from any point z_s. However, there are choices that are more convenient than others, exactly like in laser physics the waist plane is privileged with respect to others. The most convenient choice of z_s is the one that allows maximal simplification of the phase contained in the far-zone field $\widetilde{E}(\vec{\theta})$ with the quadratic phase factor in θ^2 in Eq. (16). In practical situations of interest it is possible to choose z_s in such a way that the field at the virtual source exhibits a plane wavefront, exactly as for the waist of a laser beam. Finally, in some cases, it is convenient to consider the far zone field $\widetilde{E}(\vec{\theta})$ as a superposition of different contributions. In this way, more than one virtual source can be identified and treated independently, provided that different contributions are finally summed together.

III. The third, and final step, consists in the propagation of the field from the virtual sources in paraxial approximation. Each source $\vec{\vec{E}}(z_s, \vec{r})$ generates the field

$$\vec{\vec{E}}(z, \vec{r}) = \frac{i\omega}{2\pi c(z - z_s)} \int d\vec{r'}\, \vec{\vec{E}}(z_s, \vec{r'}) \exp\left[\frac{i\omega \left|\vec{r} - \vec{r'}\right|^2}{2c(z - z_s)}\right], \tag{17}$$

as follows directly from Eq. (14). Note that here we assume $z > z_s$.

It should be stressed that the inverse field problem, which relies on far-field data only, cannot be solved without application of the paraxial approximation.

If the paraxial approximation were not applicable, we should have solved the homogeneous version of Eq. (2). Boundary conditions would have been constituted by the knowledge of the field on a open surface (for example, a transverse plane) and additionally, by Rayleigh-Sommerfeld radiation condition at infinity, separately for all polarization components of the field. However, this would not have been enough to reconstruct the field at any position in space. In order to do so, we would have had to specify the sources. In fact, the boundary conditions specified above allow one to solve the direct transmission problem, but not the inverse one.

Since, however, the paraxial approximation is applicable, the inverse field problem turns out to have unique and stable solution. A conservative estimate of the accuracy of the paraxial approximation is related to the distance d between the point where we want to know the field and the electron trajectory in the space-frequency domain [16].

The fact that we can reconstruct the near-zone field starting from the knowledge of the far-zone field and from the propagation equation looks paradoxical. In fact, in the far zone, all information about the velocity field in the Lienard-Wiechert expressions for the field is lost. It is interesting to note, for example, what is reported in [28] concerning the velocity term: "In the case of infrared synchrotron radiation, and THz radiation in particular, this term is not small and must be included in all calculations". Here we apparently seem to have lost track of every information about the velocity term. As shown in [16], the paradox is solved by the fact that, although in the far-zone limit of Eq. (12) includes information about the Fourier Transform of the acceleration term of the Lienard-Wiechert fields only, information about the velocity term is included in the field propagation equation through the Green's function Eq. (10), which solves Maxwell's equations as the Lienard-Wiechert expressions do.

4 Sharp-edge approximation

Let us consider the system depicted in Fig. 1(a). In this case of study the trajectory and, therefore, the space integration in Eq. (13) can be split in three parts: the two bends, which will be indicated with b_1 and b_2, and the straight section AB. One may write

$$\vec{\widetilde{E}}(z, \vec{r}) = \vec{\widetilde{E}}_{b1}(z, \vec{r}) + \vec{\widetilde{E}}_{AB}(z, \vec{r}) + \vec{\widetilde{E}}_{b2}(z, \vec{r}) \ , \tag{18}$$

with obvious meaning of notation. We will denote the length of the segment AB with L. This means that points A and B are located at longitudinal coordinates $z_A = -L/2$ and $z_B = L/2$.

Recalling the geometry in Fig. 1(a) we have $\gamma_z(z) = \gamma$ for $z_A < z' < z_B$. With the help of Eq. (13) we write the contribution from the straight line AB

$$\vec{\widetilde{E}}_{AB} = \frac{i\omega e}{c^2 z} \int\limits_{-L/2}^{L/2} dz' \vec{\theta} \exp\left\{\frac{i\omega}{c}\left[\frac{\theta^2 z}{2} + \frac{z'}{2}\left(\frac{1}{\gamma^2} + \theta^2\right)\right]\right\} , \tag{19}$$

where we assumed that $\vec{r}_0(z') = 0$, i.e. that the particle has zero offset and deflection. From Eq. (19) one obtains:

$$\vec{\widetilde{E}}_{AB} = \frac{i\omega e L}{c^2 z} \exp\left[\frac{i\omega\theta^2 z}{2c}\right] \vec{\theta} \,\mathrm{sinc}\left[\frac{\omega L}{4c}\left(\theta^2 + \frac{1}{\gamma^2}\right)\right] . \tag{20}$$

Note that Eq. (20) describes a spherical wave with the center in the middle of the straight section. Moreover, it explicitly depends on L.

In the previous Section we defined the formation length as the length needed for the phase of the electric field seen by an observer on the z axis to overtake the phase of the sources of a radiant. It follows from this definition, and from the phase in Eq. (19) that the formation length L_f for the straight section AB can be written as $L_f \sim \min[\gamma^2 \lambdabar, L]$. Then, either $L_f \sim \gamma^2 \lambdabar$ or $L_f \sim L$. In both cases, with the help of the phase in the integrand in Eq. (19) we can formulate on a purely mathematical basis an upper limit to the value of the observation angle of interest for the straight line, $\theta_{x,y}^2 \lesssim \lambdabar / L_f$. Moreover, if $L_f \sim \gamma^2 \lambdabar$, the maximal angle of interest is independent of the frequency and equal to $1/\gamma$, in agreement with what has been said before.

According to the superposition principle, one should sum the contribution due to the straight section to that from the bends. However, as discussed in Section 2, when $\delta \ll 1$ one can ignore the presence of the bending magnets with good accuracy. Note that a direct confirmation of this fact can be given by analyzing explicitly the field from the half bends, e.g. $\vec{\widetilde{E}}_{b2}$. An expression for the quantity $\vec{\widetilde{E}}_{b2}$ can be found from first principles, applying Eq. (13) to the case of a half bend.

In the framework of the paraxial approximation we obtain for $z > L/2$:

$$s(z) \simeq z + \frac{(z - L/2)^3}{6R^2} \quad , \quad \vec{r}(s) = -R\left[1 - \cos\left(\frac{s - L/2}{R}\right)\right]\vec{e}_x \; , \tag{21}$$

$\vec{e}_x$ (or $\vec{e}_y$) being a unit vector along the x (or y) direction. Substitution in Eq. (13) and use of Eq. (8) gives [3] :

[3] Usually, in textbooks, the z axis is chosen in such a way that $\theta_x = x/z = 0$, i.e. it is not fixed, but depends on the observer position. This can always be done, and simplifies calculations. However, since the wavefront is not spherical, this way of proceeding can hardly help to obtain the phase of the field distribution on a plane perpendicular to a *fixed* z axis. Calculations in our (fixed) coordinate system is more complicated and can be found in e.g. in [29]. After some algebraic manipulation

$$\vec{\vec{E}}_{b2}(z,\vec{\theta}) = \frac{i\omega e}{c^2 z} \exp\left[i\Phi_s\right] \exp\left[i\Phi_0\right] \int_{R\theta_x}^{\infty} dz' \left(\frac{z'}{R}\vec{e}_x + \theta_y \vec{e}_y\right)$$
$$\times \exp\left\{\frac{i\omega}{c}\left[\frac{z'}{2\gamma^2}\left(1+\gamma^2\theta_y^2\right) + \frac{z'^3}{6R^2}\right]\right\} , \tag{22}$$

where

$$\Phi_s = \frac{\omega z(\theta_x^2+\theta_y^2)}{2c} \quad \text{and}$$
$$\Phi_0 = -\frac{\omega R\theta_x}{2c}\left(\frac{1}{\gamma^2} + \frac{\theta_x^2}{3} + \theta_y^2\right) + \frac{\omega L}{4c}\left(\frac{1}{\gamma^2} + \theta_x^2 + \theta_y^2\right) . \tag{23}$$

Analysis of the phase term in z'^3 Eq. (22) shows that the integrand starts to exhibit oscillatory behavior within distances of order of $L_{fb} = \sqrt[3]{R^2 \lambdabar}$, that is the radiation formation length for the bending magnet at $\lambdabar \gg R/\gamma^3$. Similarly, as we have seen from Eq. (19), and has been also shown with qualitative arguments in Section 2, the formation length for the straight section amounts to $L_f = \min[L, \gamma^2 \lambdabar]$. The ratio L_{fb}/L_f is responsible for the relative weight of ER compared to bending magnet field contribution. Note that strictly speaking, when $\phi \gg 1$, L_{fb}/L_f is equal to $\delta \cdot \phi$ (and not to δ). However, $\delta \cdot \phi \ll 1$ always, to insure that $\lambdabar \gg \lambdabar_c$. As a result, in all generality, it is possible to talk about ER if and only if $\delta \ll 1$ and $\delta \cdot \phi \ll 1$ (or $\sqrt[3]{R^2 \lambdabar}/L \ll 1$, $\lambdabar/\lambdabar_c \ll 1$ in terms of dimensional parameters).

When $\delta \gtrsim 1$, one cannot talk about pure ER. One must account for bending magnet contributions as well. Then, expressions presented here for the electric field from the straight section can be seen as partial contributions, to be added to bending magnet contributions calculated elsewhere.

Although equivalent criteria are briefly discussed in [30, 31], in this paper

and change of variables we obtain Eq. (22).

we first introduced a measure of ”how sharp” the edges are through the parameter δ and, with this, we specified the region of applicability for ER theory.

It should also be noted that bending magnets at the straight section ends act like switchers, i.e. they switch on and off radiation seen by an observer. Observers see uniform intensity from a bend along the horizontal direction. However, not all parts of the trajectory contribute to the radiation seen by a given observer, because radiation contributions from different parts of the bend is highly collimated, hence the switching function. Since we are not interested in electromagnetic sources responsible for field contributions that are not seen by the observer, we may say that bends switch on and off electromagnetic sources as well.

Finally, it should be remarked that the far-zone asymptotic in Eq. (19) is valid at observation positions $z \gg L$. This is a necessary and sufficient condition for the vector $\vec{n}$ pointing from source to observer, to be considered constant. This result is independent of the formation length. When $L \lesssim \gamma^2 \lambda\!\!\!^{-}$ we can say that an observer is the far zone if and only if it is located many formation lengths away from the origin. This is no more correct when $L \gg \gamma^2 \lambda\!\!\!^{-}$. In this case the observer can be located at a distance $z \gg \gamma^2 \lambda\!\!\!^{-}$, i.e. many formation lengths away from the origin of the reference system, but still at $z \sim L$, i.e. in the near zone. As we see here, the formation length L_f is often, but not always related to the definition of the far (or near) zone. In general, the far (or near) zone is related to the characteristic size of the system, in our case L. In its turn $L_f \lesssim L$, which includes, when $\gamma^2 \lambda\!\!\!^{-} \ll L$, the situation $L_f \ll L$.

Since in the following we will only deal with a contribution of the electric field, i.e. that from the straight section $\vec{\tilde{E}}_{AB}$, from now on, for simplicity, we will omit the subscript AB.

The radiation energy density as a function of angles and frequencies ω, i.e. the spectral energy density per unit angle, can be written as

$$\frac{dW}{d\omega d\Omega} = \frac{cz^2}{4\pi^2}\left|\vec{\tilde{E}}\right|^2 , \tag{24}$$

$d\Omega$ being the differential of the solid angle Ω. Substituting Eq. (20) in Eq. (24) it follows that [5]

$$\frac{dW}{d\omega d\Omega} = \frac{e^2\omega^2L^2}{4\pi^2c^3}\theta^2 \,\mathrm{sinc}^2\left[\frac{L\omega}{4c}\left(\theta^2 + \frac{1}{\gamma^2}\right)\right] . \tag{25}$$

It is now straightforward to introduce the same normalized quantities defined in Section 2: $\vec{\hat{\theta}} = \sqrt{L/\lambdabar}\,\vec{\theta}$, and $\phi = L/(\gamma^2\lambdabar)$. We may write the spectral energy density per unit angle in normalized units as

$$\hat{I} \equiv \frac{c^3L}{\omega e^2}\left|\vec{\tilde{E}}\right|^2 , \tag{26}$$

so that

$$\hat{z}^2\hat{I} = \hat{\theta}^2 \,\mathrm{sinc}^2\left[\frac{1}{4}\left(\hat{\theta}^2 + \phi\right)\right] , \tag{27}$$

where $\hat{z} = z/L$. Eq. (27) is plotted in Fig. 6 for several values of ϕ as a function of the normalized angle $\hat{\theta}$. The natural angular unit is evidently $\sqrt{\lambdabar/L}$.

The spectral energy density per unit angle, once integrated in angles, is divergent, as one can see from $\hat{z}^2\hat{I} \propto 1/\hat{\theta}^2$. This feature is related with the limit of applicability of the sharp-edge approximation. Note that within the framework of the paraxial approximation alone, the integrated spectral

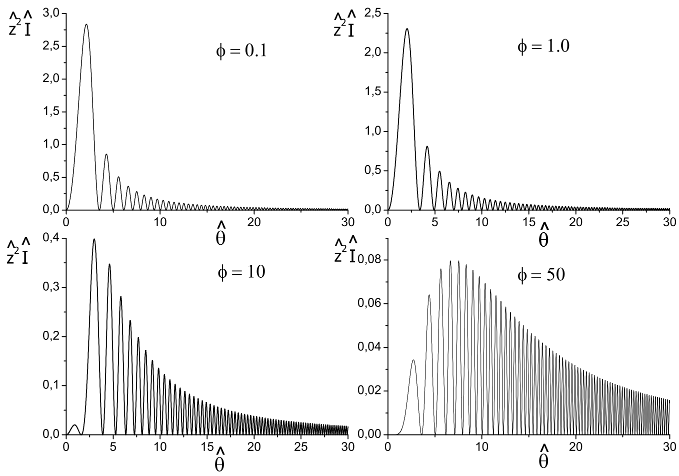

Fig. 6. Normalized spectral energy density per unit angle of the radiation from the setup in Fig. 1(a) for different values of ϕ.

energy density per unit angle calculated with Eq. (13) does not have any singularity, whatever the electron trajectory is. The paraxial approximation, as discussed above, is related to the large parameter γ^2. However, our ER theory is related to another parameter, $\delta \ll 1$, which controls the accuracy of the sharp-edge approximation. It is within the framework of the sharp-edge approximation that the integrated spectral energy density per unit angle is logarithmically divergent. Accounting for the presence of the bend would simply cancel this divergence.

We can now justify findings in the previous Section. From Eq. (27) we see that, in the limit for $\phi \ll 1$, the radiation profile is a universal function, and peaks at $\hat{\theta} \sim 2.2$. When, instead, $\phi \gtrsim 1$, radiation is much better collimated peaking at $\hat{\theta} \sim \sqrt{\phi}$ corresponding to $\theta \sim 1/\gamma$.

The behavior of the far-field emission described here is well-known in literature. Nonetheless, the accuracy of the asymptotic expression for $\delta \ll 1$,

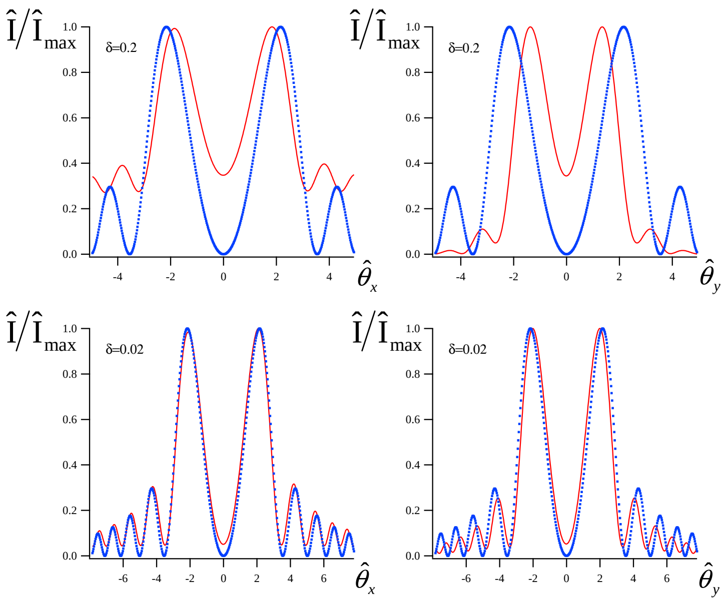

Fig. 7. Spectral energy density per unit angle as a function of the normalized angle $\hat{\theta}$ for two different edge length parameters $\delta = 0.2$ and $\delta = 0.02$. Here the straight section length parameter $\phi \simeq 0.01$. Left and right plots are obtained cutting the profile of the spectral energy density per unit angle at $\hat{\theta}_y = 0$ and $\hat{\theta}_x = 0$ respectively (i.e. electron motion is in xz plane). The dotted curves are calculated with the analytical formula Eq. (27). Solid lines are the results of numerical calculations with computer code SRW.

Eq. (27), has never been discussed: the parameter δ has been introduced here for the first time. Numerical calculations were never used before to scan the parameter space in δ and to provide an universal algorithm for estimating the accuracy of the ER theory. We can study such accuracy now by comparing asymptotical results with SRW outcomes at different values of δ. This comparison is illustrated in Fig. 7. It can be seen that edge radiation approximation provides good accuracy for $\delta \lesssim 0.01$.

For completeness, and within the limiting case for $\delta \ll 1$, it is interesting to study the accuracy of the asymptotic expression for $\phi \ll 1$ of Eq. (27).

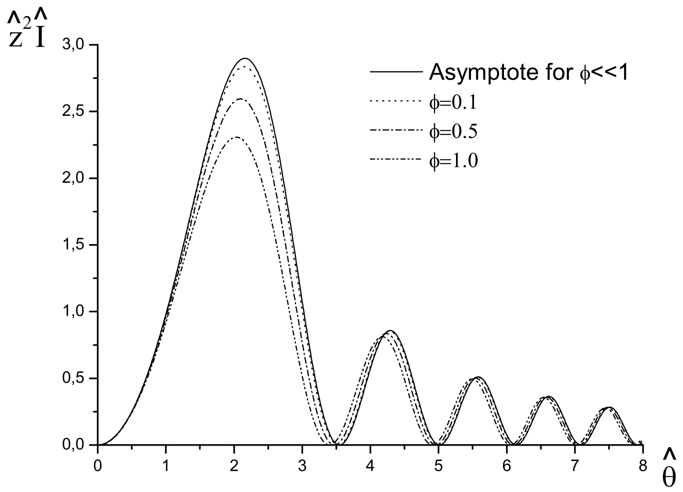

Fig. 8. Spectral energy density per unit angle as a function of the normalized angle $\hat{\theta}$ for different straight-section length parameters ϕ calculated after Eq. (27) and comparison with the asymptotic limit for $\phi \ll 1$ in Eq. (28).

In this case one does not need comparisons with SRW results, because the asymptotic limit of Eq. (27) is simply

$$\hat{z}^2 \hat{I} = \hat{\theta}^2 \, \mathrm{sinc}^2\left[\frac{\hat{\theta}^2}{4}\right] . \tag{28}$$

Results are shown in Fig. 8. It can be seen that the asymptotic expression Eq. (28) provides good accuracy for $\phi \lesssim 0.1$.

From now on, we will only consider the asymptote for sharp-edges $\delta \ll 1$ in the far-zone. This is the starting point for further investigations of near-zone ER, based on the use of virtual source techniques.

5 Near field Edge Radiation theory

5.1 Edge Radiation as a field from a single virtual source

Eq. (16) and Eq. (20) allow one to characterize the virtual source through

$$\vec{\widetilde{E}}(0,\vec{r}) = -\frac{\omega^2 eL}{2\pi c^3}\int d\vec{\theta}\,\vec{\theta}\,\mathrm{sinc}\left[\frac{\omega L}{4c}\left(\theta^2+\frac{1}{\gamma^2}\right)\right]\exp\left[\frac{i\omega}{c}\vec{r}\cdot\vec{\theta}\right]\,. \tag{29}$$

Eq. (29) is valid in any range of parameters, i.e. for any choice of ϕ. However, the Fourier transform in Eq. (29) is difficult to calculate analytically in full generality. Simple analytical results can be found in the asymptotic case for $\phi \ll 1$, i.e. for $L/(\gamma^2 \lambda\!\!\!^{-}) \ll 1$. In this limit, the right hand side of Eq. (29) can be calculated with the help of polar coordinates. An analytic expression for the field amplitude at the virtual source can then be found and reads:

$$\vec{\widetilde{E}}(0,\vec{r}) = -i\frac{4\omega e}{c^2 L}\,\vec{r}\,\mathrm{sinc}\left(\frac{\omega r^2}{cL}\right)\,, \tag{30}$$

where $r^2 = \left|\vec{r}\right|^2$ as usual. It is useful to remark, for future use, that similarly to the far-field emission Eq. (20), also the field in Eq. (30) explicitly depends on L.

It is interesting to comment on the meaning of the phase in Eq. (30), i.e. on the factor $-i$ in front of the right hand side. Such phase is linked with the (arbitrary) choice of phase of the harmonic of the charge density at $z = 0$. In particular, such phase was chosen to be zero at $z = 0$. Propagating Eq. (30) to the far-zone, one obtains Eq. (20). In other words, the plane wavefront transforms into a spherical wavefront centered at $z = 0$. Note that there is an imaginary unit i in front of Eq. (20), meaning that an extra minus sign, i.e. a phase shift of π, results from the propagation of Eq. (30). This extra phase shift of π represent the analogous of the Guoy phase shift in laser physics, and is in agreement with our interpretation of the virtual source in Eq. (30) as the waist of a laser-like beam. Note that, while for azimuthal-symmetric beams the Guoy phase shift is known to be $\pi/2$, this result is not valid in our case where the cartesian components of the field depend on the azimuthal angle.

We define the normalized transverse position $\vec{\hat{r}} = \vec{r}/\sqrt{\lambda\!\!\!^{-} L}$. Moreover, since the source is positioned at $z = 0$, we indicate the normalized spectral energy density at the virtual source as $\hat{I}_s$, defined similarly as $\hat{I}$ in Eq. (26). It follows that

$$\hat{I}_s(\hat{r}) = 16\,\hat{r}^2 \mathrm{sinc}^2\left(\hat{r}^2\right) . \tag{31}$$

The profile in Eq. (31) can be detected (aside for scaling factors) by imaging the virtual plane with an ideal lens, and is plotted in Fig. 9.

Note that Eq. (30) describes a virtual source characterized by a plane wavefront. Application to Eq. (30) of the propagation formula, Eq. (14), allows one to reconstruct the field both in the near and in the far region. We obtain the following result:

$$\begin{aligned}\vec{\tilde{E}}(z, \vec{\theta}) = &-\frac{2e}{zc}\frac{\vec{\theta}}{\theta^2}\exp\left[\frac{i\omega z\theta^2}{2c}\right] \\ &\times\left[\exp\left(-\frac{i\omega z\theta^2}{2c(1+2z/L)}\right) - \exp\left(\frac{i\omega z\theta^2}{2c(-1+2z/L)}\right)\right] ,\end{aligned} \tag{32}$$

where we defined $\vec{\theta} = \vec{r}/z$, *independently* of the value of z. This definition makes sense whenever $z \neq 0$, and yields usual angular distributions in the far zone, for $z \gg L$. Eq. (32) solves the field propagation problem for both

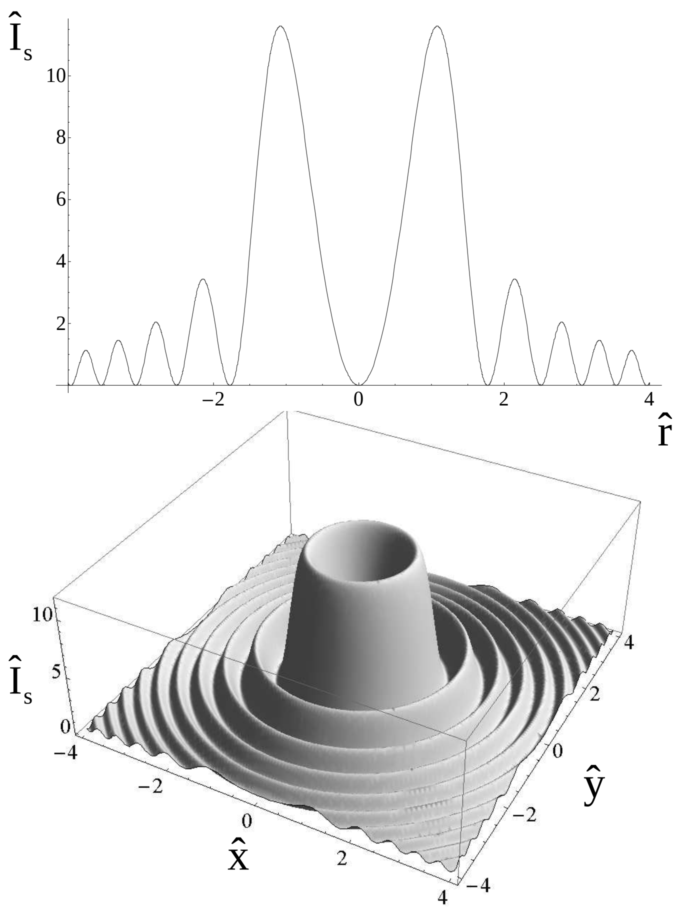

Fig. 9. Normalized spectral energy density at the virtual source, $\hat{I}_s$, as a function of $\hat{r}$ (upper plot) and 3D view as a function of $\hat{x}$ and $\hat{y}$.

the near and the far field in the limit for $\phi \ll 1$.

Eq. (32) is singular at $\vec{r} = 0$ (i.e. $\vec{\theta} = 0$) and $z = L/2$. Within our sharp-edge approximation, this singularity is mathematically related to the divergence of the integrated spectral energy density per unit angle in the far zone, which has been discussed above. If one goes beyond the applicability region of the sharp-edge approximation by specifying the nature of edges and calculating the field within the framework of the paraxial approximation alone (i.e. with Eq. (13)), one sees that the integrated spectral energy density per unit angle is not divergent anymore, and that the field reconstructed at the point $\vec{r} = 0$,

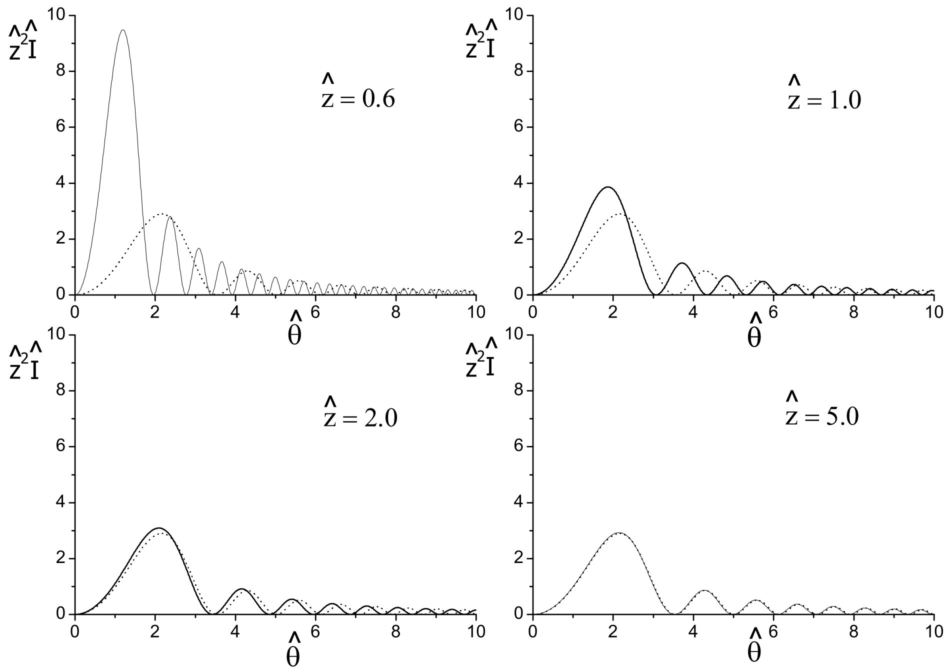

Fig. 10. Evolution of $\hat{z}^2\hat{I}$ for edge radiation in the limit for $\phi \ll 1$. These profiles, calculated with Eq. (34), are shown as a function of angles at different observation distances $\hat{z} = 0.6$, $\hat{z} = 1.0$, $\hat{z} = 2.0$ and $\hat{z} = 5.0$ (solid lines). The dashed line always refers to the far-zone asymptote, Eq. (28).

$z = L/2$ using this far-field data has no singularity at all.

Note that in the limit for $z \gg L$ Eq. (32) transforms to

$$\vec{\widetilde{E}} = \frac{i\omega e L}{c^2 z} \exp\left[\frac{i\omega\theta^2 z}{2c}\right] \vec{\theta}\, \mathrm{sinc}\left[\frac{\omega L \theta^2}{4c}\right] \tag{33}$$

corresponding to the limit of Eq. (20) for $L \ll \gamma^2 \lambda\!\!\!^{-}$, i.e. $\phi \ll 1$.

The normalized spectral energy density per unit angle associated with Eq. (32) is given by

$$\hat{z}^2\hat{I}\left(\hat{z},\hat{\theta}\right) = \frac{4}{\hat{\theta}^2}\left|\left[\exp\left(-\frac{i\hat{\theta}^2\hat{z}}{2(1+2\hat{z})}\right) - \exp\left(\frac{i\hat{\theta}^2\hat{z}}{2(-1+2\hat{z})}\right)\right]\right|^2 . \qquad (34)$$

This notation is particularly suited to discuss near and far zone regions. Eq. (34) reduces to Eq. (28) when $\hat{z} \gg 1$. To sum up, when $\phi \ll 1$ we have only two regions of interest with respect to $\hat{z}$:

- **Far zone.** In the limit for $\hat{z} \gg 1$ one has the far field case, and Eq. (34) simplifies to Eq. (28).
- **Near zone.** When $\hat{z} \lesssim 1$ instead, one has the near field case, and Eq. (34) must be used.

Of course, it should be stressed that in the case $\hat{z} \lesssim 1$ we still hold the assumption that the sharp-edge approximation is satisfied. It is interesting to study the evolution of the normalized spectral energy density per unit angle for edge radiation along the longitudinal axis. This gives an idea of how good the far field approximation ($\hat{z} \gg 1$) is. A comparison between $\hat{z}^2\hat{I}$ at different observation points is plotted in Fig. 10.

The case $\phi \ll 1$ studied until now corresponds to a short straight section, in the sense that $L \ll \gamma^2 \lambda\!\!\!^{-}$. When this condition is not satisfied, we find that the integral on the right hand side of Eq. (29) is difficult to calculate analytically. Thus, the single-source method used here is advantageous in the case $\phi \ll 1$ only. However, one can use numerical techniques to discuss the case for any value of ϕ. With the help of polar coordinates, the right hand side of Eq. (29) can be transformed in a one-dimensional integral, namely

$$\vec{\widetilde{E}}(0,\vec{r}) = -\frac{4i\omega e}{c^2}\frac{\vec{r}}{r}\int_0^\infty \frac{\theta^2}{\theta^2+1/\gamma^2}\sin\left[\frac{\omega L}{4c}\left(\theta^2+\frac{1}{\gamma^2}\right)\right]J_1\left(\frac{\omega\theta r}{c}\right)d\theta \,, \qquad (35)$$

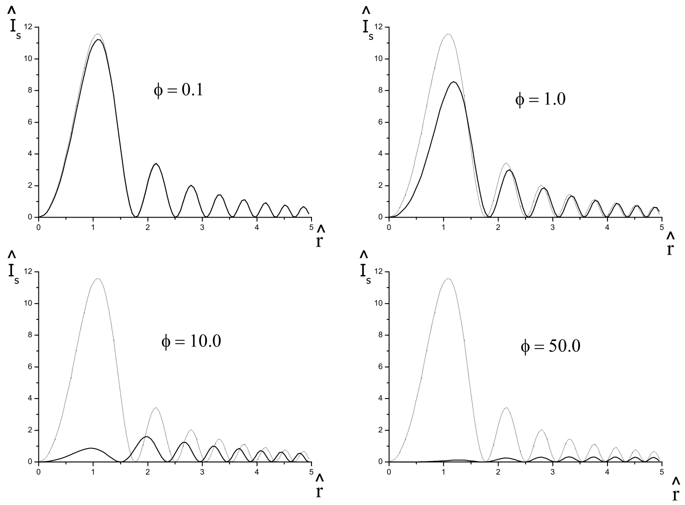

Fig. 11. Normalized spectral energy density at the virtual source for the setup in Fig. 1(a). These profiles are shown for ϕ = 0.1, ϕ = 1.0, ϕ = 10.0 and ϕ = 50.0 (solid lines). Solid curves are calculated with the help of Eq. (35). The dotted lines show comparison with the asymptotic limit for $\phi \ll 1$, shown in Fig. 9 and calculated using Eq. (31).

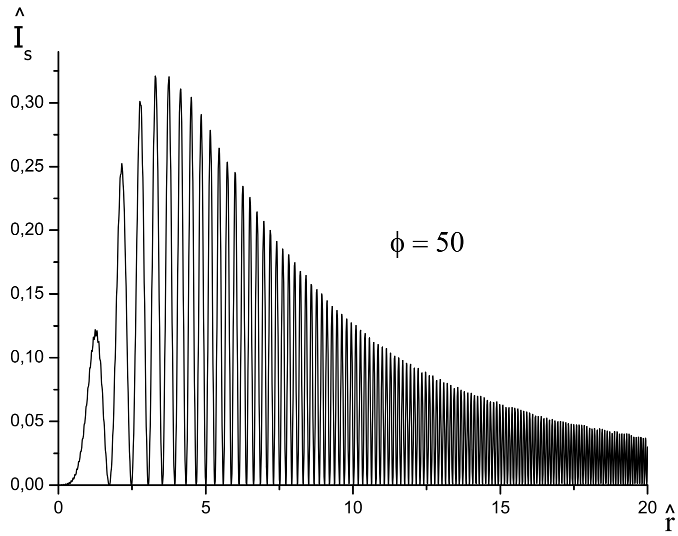

Fig. 12. Normalized spectral energy density at the virtual source for the setup in Fig. 1(a) for ϕ = 50 (enlargement of the bottom right graph in Fig. 11).

yielding

$$\hat{I}_s(\hat{r}) = \left|\int_0^\infty \frac{4\hat{\theta}^2}{\hat{\theta}^2+\phi}\sin\left[\frac{\hat{\theta}^2+\phi}{4}\right]J_1\left(\hat{\theta}\hat{r}\right)d\hat{\theta}\right|^2 . \tag{36}$$

We calculated the spectral energy density associated with the virtual source for values $\phi = 0.1$, $\phi = 1$, $\phi = 10$ and $\phi = 50$, the same values chosen for Fig. 6. We plot these distributions in Fig. 11. It is also instructive to make a separate, enlarged plot of the case $\phi = 50$, that is in the asymptotic case for $\phi \gg 1$. This is given in Fig. 12. Fine structures are now evident, and are consistent with the presence of fine structures in Fig. 6 for the far zone.

We managed to specify the field at the virtual source by means of numerical techniques, even in the case $\phi \gg 1$ (see Fig. 12). Once the field at the virtual source is specified for any value of ϕ, Fourier Optics can be used to propagate it. However, we prefer to proceed following another path. There is, in fact, an alternative way to obtain the solution to the field propagation problem valid for any value of ϕ, and capable of giving a better physical insight for large values of ϕ.

5.2 *Edge Radiation as a superposition of the field from two virtual sources*

Consider the far field in Eq. (20). This can also be written as

$$\vec{\bar{E}}\left(z,\vec{\theta}\right) = \vec{\bar{E}}_1\left(z,\vec{\theta}\right) + \vec{\bar{E}}_2\left(z,\vec{\theta}\right) \ \ , \tag{37}$$

where

$$\vec{\bar{E}}_{1,2}\left(z,\vec{\theta}\right) = \mp\frac{2e\vec{\theta}}{cz(\theta^2+1/\gamma^2)}\exp\left[\mp\frac{i\omega L}{4c\gamma^2}\right]\exp\left[\frac{i\omega L\theta^2}{2c}\left(\frac{z}{L}\mp\frac{1}{2}\right)\right]. \tag{38}$$

When $z \gg L$, the two terms $\vec{\widetilde{E}}_1$ and $\vec{\widetilde{E}}_2$ represent two spherical waves respectively centered at $z_{s1} = -L/2$ and $z_{s2} = L/2$, that is at the edges between straight section and bends[4]. Analysis of Eq. (38) shows that both contributions to the total field are peaked at an angle of order $1/\gamma$. While the amplitude of the total field explicitly depends on L, the two expressions $\vec{\widetilde{E}}_1$ and $\vec{\widetilde{E}}_2$ exhibit dependence on L through phase factors only. This fact will have interesting consequences, as we will discuss later. The two spherical waves represented by $\vec{\widetilde{E}}_1$ and $\vec{\widetilde{E}}_2$ may be thought as originating from two separate virtual sources located at the edges between straight section and bends. One may then model the system with the help of two separate virtual sources, and interpret the field at any distance as the superposition of the contributions from two edges. It should be clear that contributions from these edges are linked with an integral of the trajectory followed by the electron. Thus the word ”edge” should be considered as a synonym for ”virtual source” here.

Let us specify analytically the two virtual sources at the edges of the setup. To this purpose, we take advantage of Eq. (16) with $z_s = z_{s(1,2)}$, separately substituting $\vec{\widetilde{E}}_1$ and $\vec{\widetilde{E}}_2$ and using polar coordinates. We find the following

[4] At first glance this statement looks counterintuitive. In order to find where the spherical wave is centered, one needs to know where the phase becomes zero. Now, when $z = L/2$, the phase in θ^2 for $\vec{\widetilde{E}}_2$ in Eq. (38) is not zero, hinting to the fact that the spherical wave $\vec{\widetilde{E}}_2$ is not centered at $z = L/2$. This last observation, however, is misleading. In fact, one should account for the fact that the definition $\vec{\theta} = \vec{r}/z$ is not natural for $\vec{\widetilde{E}}_1$ and $\vec{\widetilde{E}}_2$. In fact, according to it, $\vec{\theta}$ is measured from the center of the straight section, while it should be measured from $z = -L/2$ for $\vec{\widetilde{E}}_1$ and from $z = L/2$ for $\vec{\widetilde{E}}_2$. Also note that Eq. (38) is only valid in the limit $z \gg L$.

expressions for the field at the virtual source positions $z_{s1} = -L/2$ and $z_{s2} = L/2$:

$$\vec{\widetilde{E}}_{s1,s2}\left(\mp\frac{L}{2},\vec{r}\right) = \pm\frac{2\omega e}{c^2\gamma}\exp\left[\mp\frac{i\omega L}{4\gamma^2 c}\right]\frac{\vec{r}}{r}K_1\left(\frac{\omega r}{c\gamma}\right) , \tag{39}$$

where $K_1(\cdot)$ is the modified Bessel function of the first order. Analysis of Eq. (39) shows a typical scale related to the source dimensions of order $\bar{\lambda}\gamma$ in dimensional units, corresponding to $1/\sqrt{\phi}$ in normalized units. Also, the fact that the field in the far zone, Eq. (20), exhibits dependence on L only through phase factors implies that the field at the virtual sources, Eq. (39), exhibits dependence on L only through phase factors (and viceversa).

Application of the propagation formula Eq. (14) allows to calculate the field at any distance z in free-space. Of course, Eq. (39) can also be used as input to any Fourier code to calculate the field evolution in the presence of whatever optical beamline. However, here we restrict ourselves to the free-space case. In order to simplify the presentation of the electric field we take advantage of polar coordinates and we use the definition $\vec{\hat{E}} \equiv \vec{\widetilde{E}}\sqrt{\bar{\lambda}L}\ c/e$ (so that $\hat{I}$, introduced in Eq. (26), is given by $\hat{I} = |\vec{\hat{E}}|^2$) for the field in normalized units. We obtain:

$$\begin{aligned}\vec{\hat{E}}\left(\hat{z},\vec{\hat{\theta}}\right) = &\left\{\frac{\vec{\hat{\theta}}}{\hat{\theta}}\frac{2\sqrt{\phi}\exp\left[i\phi/4\right]}{\hat{z}-1/2}\exp\left[\frac{i\hat{\theta}^2\hat{z}^2}{2\left(\hat{z}-1/2\right)}\right]\right.\\ &\left.\times\int_0^\infty d\hat{r}'\hat{r}'K_1\left(\sqrt{\phi}\hat{r}'\right)J_1\left(\frac{\hat{\theta}\hat{r}'\hat{z}}{\hat{z}-1/2}\right)\exp\left[\frac{i\hat{r}'^2}{2\left(\hat{z}-1/2\right)}\right]\right\}\\ &-\left\{\frac{\vec{\hat{\theta}}}{\hat{\theta}}\frac{2\sqrt{\phi}\exp\left[-i\phi/4\right]}{\hat{z}+1/2}\exp\left[\frac{i\hat{\theta}^2\hat{z}^2}{2\left(\hat{z}+1/2\right)}\right]\right.\\ &\left.\times\int_0^\infty d\hat{r}'\hat{r}'K_1\left(\sqrt{\phi}\hat{r}'\right)J_1\left(\frac{\hat{\theta}\hat{r}'\hat{z}}{\hat{z}+1/2}\right)\exp\left[\frac{i\hat{r}'^2}{2\left(\hat{z}+1/2\right)}\right]\right\} .\end{aligned} \tag{40}$$

In the limit for $\hat{z} \gg 1$, using Eq. (40) and recalling $\int_0^\infty d\hat{r}'\ \hat{r}' K_1(\sqrt{\phi}\hat{r}')J_1(\hat{\theta}\hat{r}') = \hat{\theta}/[\sqrt{\phi}(\hat{\theta}^2 + \phi)]$ we obtain back Eq. (27). Similarly, in the limit for $\phi \ll 1$, and using the fact that $K_1(\sqrt{\phi}\hat{r}) \simeq 1/(\hat{r}\sqrt{\phi})$ one recovers Eq. (32). In general, the integrals in Eq. (40) cannot be calculated analytically, but they can be integrated numerically.

5.3 *Classification of regions of observation*

Qualitatively, we can deal with two limiting cases of the theory, the first for $\phi \ll 1$ and the second for $\phi \gg 1$. As for the case of a single virtual source, there are no constraints, in principle, on the value of ϕ. However, as we will see, the two-source method gives peculiar advantages in the case $\phi \gg 1$, while, has we have seen before, the case $\phi \ll 1$ is better treated in the framework of a single source.

5.3.1 *Case $\phi \ll 1$*

Let us briefly discuss the case $\phi \ll 1$ in the framework of the two-source method. In this case, one obviously obtains back Eq. (32). An alternative derivation has been shown in Section 5.1. As one can see, Eq. (32) is independent of ϕ. In Fig. 10 we plotted results for the propagation according to Eq. (34). Radiation profiles are shown as a function of angles $\hat{\theta}$ at different observation distances $\hat{z} = 0.6$, $\hat{z} = 1.0$, $\hat{z} = 2.0$ and $\hat{z} = 5.0$. As discussed before, one can recognize two observation zones of interest: the near and the far zone. As it can be seen from Eq. (32), the total field is given, both in the near and in the far zone, by the interference of the virtual source contributions. The virtual sources themselves are located at the straight section edges. Eq.

(40) shows that the transverse dimension of these virtual sources is given by $\gamma\lambda\!\!\!^{-}$ in dimensional units. This is the typical scale in r' after which the integrands in $d\hat{r}'$ in Eq. (40) are suppressed by the function K_1. Thus, the sources at the edges of the straight section have a dimension that is independent of L. In the center of the setup instead, the virtual source has a dimension of order $\sqrt{\lambda\!\!\!^{-} L}$ as it can be seen Eq. (31). When $\phi \ll 1$ the source in the center of the setup is much smaller than those at the edge. This looks paradoxical. The explanation is that the two contributions due to edge sources interfere in the center of the setup. In particular, when $\phi \ll 1$ they nearly compensate, as they have opposite sign. As a result of this interference, the single virtual source in the center of the setup (and its far-zone counterpart) has a dimension dependent on L (in non-normalized units) while for two virtual sources at the edges (and in their far-zone counterpart) the dependence on L is limited to phase factors only. Due to the fact that edges contributions nearly compensate for $\phi \ll 1$ one may say that the single-source picture is particularly natural in the case $\phi \ll 1$.

5.3.2 *Case $\phi \gg 1$*

Let us now discuss the case $\phi \gg 1$. In this situation the two-sources picture becomes more natural. We indicate with $d_{1,2} = z \pm L/2$ the distances of the observer from the edges. From Eq. (19) we know that when $\phi \gg 1$ the formation length is $L_f = \gamma^2\lambda\!\!\!^{-}$, much shorter than the system dimension L. As a result, one can recognize four regions of observation of interest.

In Fig. 13 we plotted, in particular, results for the propagation in case $\phi = 50$. In this case, for arbitrary $\hat{z}$, integrals in Eq. (40) cannot be calculated

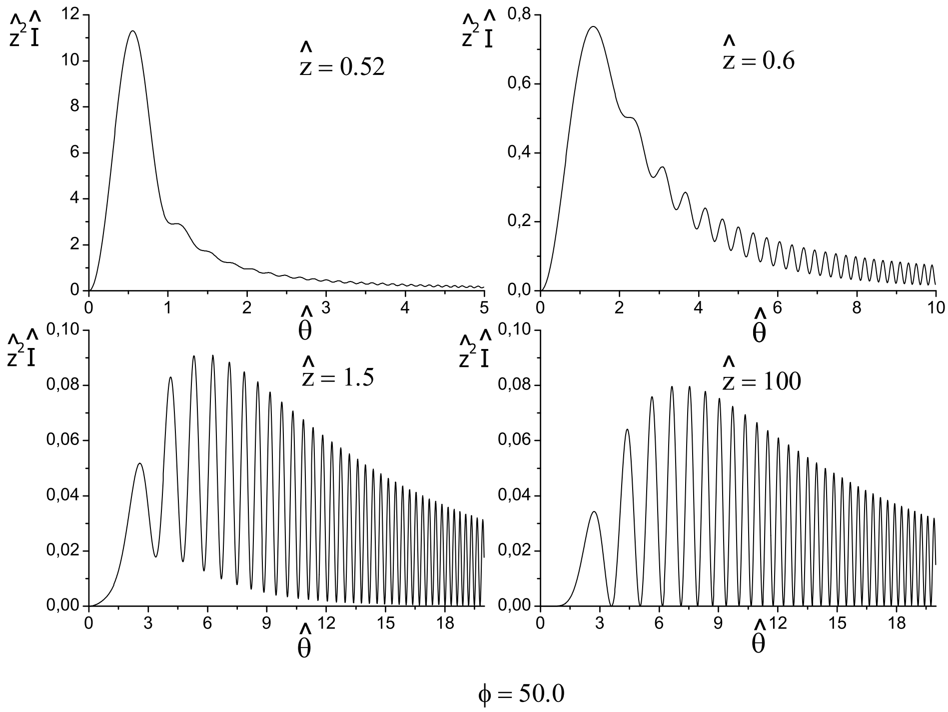

Fig. 13. $\hat{z}^2\hat{I}$ at $\phi = 50$. These profiles are shown as a function of angles at different observation distances $\hat{z} = 0.52$, $\hat{z} = 0.6$, $\hat{z} = 1.5$ and $\hat{z} = 100.0$.

analytically, but they can be integrated numerically. Radiation profiles are shown as a function of angles $\hat{\theta}$ at different observation distances $\hat{z} = 0.52$, $\hat{z} = 0.6$, $\hat{z} = 1.5$ and $\hat{z} = 100.0$.

- **Two-edge radiation, far zone:** $d_{1,2} \gg L$ **(i.e.** $z \gg L$**). Eq. (20) and Eq. (25) should be used.** When $d_{1,2} \gg L$ we are summing far field contributions from the two edge sources. This case is well represented in Fig. 13 for $\hat{z} = 100$, where interference effects between the two edges contribution are clearly visible.
- **Two-edge radiation, near zone:** $d_{1,2} \sim L$**. Eq. (40) should be used.** When $d_{1,2} \sim L$ the observer is located far away with respect to the formation length of the sources. Both contributions from the sources are important,

but that from the nearest source begins to become the main one, as d_1 and d_2 become sensibly different. This case is well represented in Fig. 13 for $\hat{z} = 1.5$.

- **Single-edge radiation, far zone: $\gamma^2 \lambda\!\!\!^{-} \ll d_2 \ll L$ and $r \ll L/\gamma$. Eq. (41) should be used.** When $\gamma^2 \lambda\!\!\!^{-} \ll d_2 \ll L$, the contribution due to the near edge becomes more and more important. Such tendency is clearly depicted in Fig. 13 for $\hat{z} = 0.6$. Interference tends to disappear as the near edge becomes the dominant one. In this case, one finds that the electric field in Eq. (40) reduces to

$$\vec{\widetilde{E}}\left(z, \vec{\xi}\right) = \frac{2e\gamma^2 \vec{\xi}}{c(z - L/2)(\gamma^2\xi^2 + 1)} \exp\left[\frac{i\omega L}{4c\gamma^2}\right] \exp\left[\frac{i\omega L \xi^2}{2c}\left(\frac{z}{L} - \frac{1}{2}\right)\right] , \quad (41)$$

where $\xi = r/(z - L/2) = r/d_2$. Note that ξ is used here in place of θ, because by definition $\theta = r/z$, where z is calculated from the center of the straight section, whereas the definition of ξ is related to the edge position at $z = L/2$. It should be remarked that Eq. (41) constitutes the field contribution from the downstream edge of the straight section, and that the contribution from the upstream edge (at $z = -L/2$) can be found from Eq. (41) by performing everywhere in Eq. (41), i.e. also in ξ, the substitution $L/2 \longrightarrow -L/2$, and by changing an overall sign. Eq. (41) corresponds to a spectral energy density per unit angle [5]

$$\frac{dW}{d\omega d\Omega} = \frac{e^2}{c\pi^2} \frac{\gamma^4\xi^2}{\left(\gamma^2\xi^2 + 1\right)^2} . \quad (42)$$

It is important to specify the region of applicability of Eq. (41) in the transverse direction. For a single edge in the far zone, the amplitude of the field decreases as r^{-1}, as can be checked by substituting the definition of $\vec{\xi}$ in Eq. (41), and does not depend on z nor γ for angles of observation larger than $1/\gamma$. Since $d_2 \ll L$, such dependence holds for the upstream edge at

$r \gtrsim L/\gamma$, and for the downstream edge at $r \sim d_2/\gamma \ll L/\gamma$. As a result, for $r \gtrsim L/\gamma$, the contributions from the two edges are comparable, and a single-edge asymptote cannot be used. It follows that Eq. (41) applies for $r \ll L/\gamma$.

- **Single-edge radiation, near zone: $\sqrt[3]{\lambda\!\!\!^{-} R^2} \ll d_2 \lesssim \gamma^2 \lambda\!\!\!^{-}$, $r \ll \gamma \lambda\!\!\!^{-}$. Eq. (43) should be used.** When $\sqrt[3]{\lambda\!\!\!^{-} R^2} \ll d_2 \lesssim \gamma^2 \lambda\!\!\!^{-}$ we have the contribution from a single edge in the near zone.

As d_2 becomes smaller and smaller the maximum in the radiation profile increases (see Fig. 13). This behavior is to be expected. In fact, on the one hand the virtual source exhibits a singular behavior at $r = 0$, while on the other hand the integral in Eq. (14) must reproduce the virtual source for $z \longrightarrow z_s$. In other words, for $z \longrightarrow z_s$, the propagator must behave like a Dirac δ-distribution. However, the way such asymptote is realized is not trivial. At any finite distance d_2 from the source, Eq. (14) eliminates the singularity of the Bessel K_1 function. This means that the maximum value in $|\vec{\widetilde{E}}|^2$ increases as d_2 decreases, but it always remains finite. In particular, at $\vec{r} = 0$, $|\vec{\widetilde{E}}|^2 = 0$. However, by conservation of energy the integral of $|\vec{\widetilde{E}}|^2 = 0$ over transverse coordinate must diverge at any finite distance from the source, because the field diverges at the source position.

Note that when $r \ll \gamma \lambda\!\!\!^{-}$ and $d_2 \ll \gamma^2 \lambda\!\!\!^{-}$, the integral pertaining the near (downstream) edge (at $z_{s2} = L/2$) in Eq. (40) can be calculated analytically. In fact, the Bessel K_1 function in the integrand can be expanded for small values of the argument when $\hat{r}' \ll 1/\sqrt{\phi}$. When this is not the case ($\hat{r}' \gtrsim 1/\sqrt{\phi}$) the phase factor under the integral sign makes the integrand exhibiting oscillatory behavior (because $\hat{z} - 1/2 \ll 1/\phi$, since $d_2\theta \ll \gamma^2 \lambda\!\!\!^{-}$). Contributions to the integrals are therefore negligible. As a result, in this case one can use the expansion $K_1(\sqrt{\phi}\hat{r}') \sim 1/(\sqrt{\phi}\hat{r}')$. Then, using the fact that $\int_0^\infty dx J_1(Ax)\exp[iBr^2] = 1/A\{1-\exp[-iA^2/(4B)]\}$ (for A and B positive), one obtains [8]

$$\vec{\widetilde{E}}\left(z,\vec{\xi}\right) = \frac{2ie\vec{\xi}}{c\xi^2(z-L/2)}\exp\left[\frac{i\omega L}{4c\gamma^2}\right]\exp\left[\frac{i\omega\xi^2(z-L/2)}{4c}\right] \times \sin\left[\frac{\omega\xi^2(z-L/2)}{4c}\right]. \quad (43)$$

Note that while the modulus of Eq. (43) is independent of ϕ, its region of applicability is related to ϕ and the asymptotic expression deviates from Eq. (40) for smaller value of $\hat{\theta}$ when ϕ is larger. In fact, Eq. (43) is valid only when $\hat{z} - 1/2 \ll 1/\phi$ and $\hat{z}\hat{\theta} \ll 1/\sqrt{\phi}$ (i.e. $r \ll \gamma\lambdabar$ and $d_2 \ll \gamma^2\lambdabar$).

It is interesting to remark here that Eq. (32), which was derived for $\phi \ll 1$, reduces to Eq. (43) when $d_2 \ll L$ and $r \ll \sqrt{\lambdabar L}$. It follows that the validity of Eq. (43) has a wider region of applicability than that considered here. In fact, it may be applied whenever $\sqrt[3]{\lambdabar R^2} \ll d_2 \ll \min(L, \gamma^2\lambdabar)$ and $r \ll \sqrt{\lambdabar \min(L, \gamma^2\lambdabar)}$.

If we propagate Eq. (43) to the far zone we obtain an asymptote which is valid only for angles much larger than $1/\gamma$ (i.e. Eq. (43) is an asymptote for high values of spatial frequencies). The modulus of Eq. (43) does not depend on γ (while in the non-asymptotic case radiation for any value of z must depend on γ, because the far-field radiation from a single edge depends on γ too) nor it includes information about distribution in the far zone within angles comparable with $1/\gamma$. Thus, the applicability of this high spatial-frequency asymptote depends on what practical (or theoretical) problem we try to solve. It is useful, for example, if we discuss about a sample in the very near zone. However, if we discuss about design of beam line with an acceptance angle comparable with $1/\gamma$ (which is equivalent to some spatial-frequency filter) the asymptotic expression in Eq. (43) cannot be applied anymore, and one should use exact results from the propagation integral, i.e. the near-field expression Eq. (40).

The above-given classification in zones of interest with asymptotical expressions for the electric field constitutes an important result of our paper. In fact, expressions for the electric field without explicit specification of their region of applicability are incomplete, and have no practical nor theoretical utility. From this viewpoint, it is interesting to compare our results with literature. We will limit our discussion to a comparison with recent review [28], which summarizes up-to-date understanding of ER within the SR community.

One result in [28] (Eq. (26)) corresponds to the square modulus of our Eq. (43), the single edge near-zone case. The region of applicability specified in [28] for such result [5] is $\lambdabar \ll d_2 \lesssim \gamma^2 \lambdabar$ and $L \longrightarrow \infty$. A first problem in applying this prescription is intrinsic in the condition $L \longrightarrow \infty$, as there is no comparison of L to any other characteristic length. Secondly, this result is independent of γ and L. As a result, it cannot be valid for arbitrary transverse distance r. In fact, since the far-zone field depends on both γ and L, should we propagate Eq. (43) in the far zone, we could never obtain an outcome dependent on γ and L. It follows that, as we discussed above, Eq. (43) is valid for arbitrary L (under the sharp-edge limit $\sqrt[3]{\lambdabar R^2} \ll L$), but its region of applicability depends on L or γ: $\sqrt[3]{\lambdabar R^2} \ll d_2 \ll \min(L, \gamma^2 \lambdabar)$ and $r \ll \sqrt{\lambdabar \min(L, \gamma^2 \lambdabar)}$. Note that the requirement $r \ll \lambdabar\gamma$ for the applicability of Eq. (43) is present in the original paper [8], but has been omitted in some later publications, e.g. [9, 10, 13]. Because of this the dependence of

[5] Converted to our notation.

near-zone single-edge radiation upon γ was unclear, and the asymptotic expression Eq. (43) started to be considered by other authors, as in [28], without proper requirements on r.

A second result in [28] for the case of a finite straight section length L (Eq. (27)) corresponds to our Eq. (34). This fact can be proved with the help of straightforward mathematical steps. The region of applicability of Eq. (27) in [28] is specified by the words "under conditions of validity of equation (26)", i.e. $\lambda\!\!\!^{-} \ll d_2 \lesssim \gamma^2 \lambda\!\!\!^{-}$. In contrast to this, we have seen that Eq. (34) is valid for arbitrary $d_2 \gg \sqrt[3]{\lambda\!\!\!^{-} R^2}$, but includes limitations on L in the form: $\sqrt[3]{\lambda\!\!\!^{-} R^2} \ll L \ll \gamma^2 \lambda\!\!\!^{-}$.

The following result in [28], Eq. (28), is the far-zone single-edge result, i.e. our Eq. (42). Eq. (28) in [28] is presented without region of applicability while, as we have seen, it is valid for $\gamma^2 \lambda\!\!\!^{-} \ll d_2 \ll L$ and $r \ll L/\gamma$. Note that in this case the denomination "far zone" is not related with the usual understanding $d_2 \longrightarrow \infty$, as is the case for the usual far-zone expression for two-edges, but it includes a limit on d_2, i.e. $d_2 \ll L$.

The final result in [28] is Eq. (29), that is our far-zone two-edge case, Eq. (25). Also Eq. (29) is presented without region of applicability while, as we have seen, $d_2 \gg L$.

It should be appreciated how our analysis of ER through the parameter δ allowed us to define "how sharp" the edges are, and to specify the region of applicability for ER theory.

As a final remark, note that in literature the single edge far-zone case is usually presented as the simplest and fundamental case, while in our view

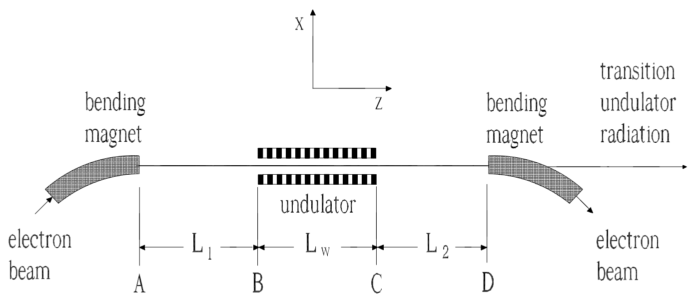

Fig. 14. Transition undulator radiation geometry.

this is the most complicated and misleading case to discuss. For the sake of exemplification, consider the usual assumption made in this case, i.e. $L \longrightarrow \infty$. In order to discuss the far-zone expression, one needs $z \longrightarrow \infty$, and comparing z to L becomes impossible. In other words, L drops out of from the problem parameters and, as in [28], it never appears in the condition for the region of applicability anymore. In contrast to this, our simplest model is the two-edge far-zone model, whose region of applicability is: $z \gg L$ (or $d_2 \gg L$). It is independent of γ and it is much easier (although an extra-limitation on angles $\theta \ll \sqrt[3]{\bar{\lambda}/R}$ should be included, due to the sharp-edge approximation). After introduction of this model, the following natural step was to generalize it to the near zone, introducing more complicated regions of applicability discussed before.

6 Transition undulator radiation

In this Section we apply the method of virtual sources to the more complicated case of an undulator setup.

Instead of the setup in Fig. 1(a), we now consider the system depicted in Fig.

14 and we consider a single particle moving along the system. The electron enters the setup via a bending magnet, passes through a straight section (segment AB), an undulator (segment BC), and another straight section (segment CD). Finally, it leaves the setup via another bend. Radiation is collected at a distance z from the center of the reference system, located in the middle of the undulator. The passage of the electron through the setup results in collimated emission of radiation in the range $\bar{\lambda} \gg \bar{\lambda}_r$ and $\bar{\lambda} \gg \bar{\lambda}_c$, where $\bar{\lambda}_r$ is the resonance wavelength of the fundamental harmonic of the undulator, i.e. the extra characteristic length introduced in the setup. This kind of radiation is known in literature as Transition Undulator Radiation (TUR) [17, 18, 9, 19, 21]. We will retain this name although, as we will see, what we are really discussing about is edge radiation from an undulator setup.

In our case of study the trajectory and, therefore, the space integration in Eq. (13) can be split in five parts: the two bends, which will be indicated with b_1 and b_2, the two straight sections AB and CD and the undulator BC. One may write

$$\vec{\widetilde{E}}(z,\vec{r}) = \vec{\widetilde{E}}_{b1}(z,\vec{r}) + \vec{\widetilde{E}}_{AB}(z,\vec{r}) + \vec{\widetilde{E}}_{BC}(z,\vec{r}) + \vec{\widetilde{E}}_{CD}(z,\vec{r}) + \vec{\widetilde{E}}_{b2}(z,\vec{r}) \ , \tag{44}$$

with obvious meaning of notation.

We will denote the length of the segment AD with L_{tot}, while we will indicate the length of the straight section AB with L_1, the length of the straight section CD with L_2 and the length of the undulator with L_w. It follows that $L_{\mathrm{tot}} = L_1 + L_w + L_2$. This means that point A is located at longitudinal coordinate $z_A = -L_1 - L_w/2$, while B, C and D are located respectively at

$z_B = -L_w/2$, $z_C = L_w/2$ and $z_D = L_w/2 + L_2$.

We will describe the field from our TUR setup as a superposition of three laser-like beam from straight sections and undulator. As before, with the help of Eq. (13) we will first derive an expression for the field in the far zone. Then we will calculate the field distribution at the virtual source with the help of Eq. (16). Finally, Eq. (17) will allow us to find an expression for the field both in the near and in the far zone.

6.1 *Far field from the undulator setup*

Let us describe the far field from the undulator setup in Fig. 14 by separately characterizing different field contributions and finally adding them together.

6.1.1 *Field contribution calculated along the undulator*

We first consider the contribution $\vec{\tilde{E}}_{BC}$ from the undulator. Assuming a planar undulator with N_w periods we write the following expression for the transverse velocity of an electron:

$$\vec{v}_\perp(z) = -\frac{cK}{\gamma} \sin(k_w z)\vec{x}\,. \tag{45}$$

Here $K = (\lambda_w e H_w)/(2\pi m_\mathrm{e} c^2)$ is the undulator parameter, m_e being the electron mass and H_w being the maximum of the magnetic field produced by the undulator on the z axis. Moreover, $k_w = 2\pi/\lambda_w$, where λ_w is the undulator period, so that the undulator length is $L_w = N_w\lambda_w$. The transverse position of the electron is

$$\vec{r}_0(z) = \frac{K}{\gamma k_w} \cos(k_w z)\vec{x} \,. \tag{46}$$

We can now substitute Eq. (46) and Eq. (45) in Eq. (13). Such substitution leads to an expression valid in the far zone. We obtain

$$\vec{\widetilde{E}}_{BC}(z, \vec{r}, \omega) = \frac{i\omega e}{c^2 z} \int_{z_B}^{z_C} dz' \exp[i\Phi_{BC}] \left\{ \left[\frac{K}{\gamma} \sin(k_w z') + \theta_x \right] \vec{x} + \theta_y \vec{y} \right\} \,. \tag{47}$$

Here

$$\Phi_{BC} = \frac{\omega}{c} \left\{ \frac{\theta^2}{2} z + \frac{z'}{2} \left(\frac{1}{\bar{\gamma}_z^2} + \theta^2 \right) - \frac{K\theta_x}{\gamma k_w} \cos(k_w z') - \frac{K^2}{8\gamma^2 k_w} \sin(2k_w z') \right\} \,, \tag{48}$$

where the average longitudinal Lorentz factor $\bar{\gamma}_z$ in Eq. (48) turns out to be $\bar{\gamma}_z = \gamma/\sqrt{1 + K^2/2}$, and is always smaller than γ because the average longitudinal velocity of the electron inside the undulator is smaller than that along the straight sections.

In this paper we will be interested up to frequencies much lower than the resonance frequency, i.e. $\lambdabar \gg \lambdabar_r$, with $\lambdabar_r = 1/(2\bar{\gamma}_z^2 k_w)$.

We can show that this condition is analogous, for TUR radiation, to condition $\phi \cdot \delta \ll 1$ for the simple edge radiation setup in Fig. 1(a). In order to do so, we first need to discuss the formation length associated with the undulator, i.e. with Eq. (47). The definition of formation length was introduced before as the value of $z_2 - z_1$ for which the right hand side of Eq. (8) is of order unity. However, the physical meaning of formation length is related with the integration range in z' such that the integrand in Eq. (47) exhibits an oscillatory behavior. In our case, not only the phase in Eq. (48), but also the $\sin(\cdot)$ term in Eq. (47) have an oscillatory character, and must be taken into account when calculating the formation length. As a result, in the long-wavelength asymptotic ($\lambdabar \gg \lambdabar_r$), we deal with a situation where the $\sin(\cdot)$ and the $\vec{\theta}$ terms in Eq. (47) have different formation lengths. From the $\sin(\cdot)$ term in Eq. (47) and from Eq. (48) follows a formation length $L_f = \lambdabar_w$, and a characteristic angle $\theta \sim \sqrt{\lambdabar/\lambdabar_w}$. However, the TUR contribution is given by the terms in θ_x and θ_y in Eq. (47). For these terms, from Eq. (48) follows a formation length $L_f \sim \min(\bar{\gamma}_z^2 \lambdabar, N_w \lambdabar_w)$, in the limit for $\lambdabar \gg \lambdabar_r$. In this limit, the TUR contribution is collimated to angles $\theta^2 \ll \lambdabar/\lambdabar_w$. Only within these conditions one can properly talk about TUR. Note that $L_f \gg \lambdabar_w$ always, because $\bar{\gamma}_z^2 \lambdabar \sim \lambdabar_w \lambdabar/\lambdabar_r \gg \lambdabar_w$ and we assume $N_w \gg 1$. The expression for the formation length L_f above is analogous to that for edge radiation, which is given by $\min(\gamma^2 \lambdabar, L)$. The analogous of the ϕ parameter is now given by $\phi_w = \lambdabar_w N_w/(\bar{\gamma}_z^2 \lambdabar)$, while the analogous of the δ parameter is $\delta_w = \lambdabar_w/(\lambdabar_w N_w) = 1/N_w \ll 1$, as $N_w \gg 1$. It follows that $\phi_w \cdot \delta_w = \lambdabar_w/(\bar{\gamma}_z^2 \lambdabar) \sim \lambdabar_r/\lambdabar \ll 1$.

For $\phi_w \cdot \delta_w \ll 1$ and $\delta_w \ll 1$ the contribution due to the term in $\sin(k_w z')$ in Eq. (47) can always be neglected when compared with the maximal field magnitude of the terms in $\theta_{x,y}$. Similarly, in Eq. (48), phase terms in $\cos(k_w z')$ and $\sin(2k_w z')$ can also be neglected. As a result, Eq. (47) can be simplified as

$$\vec{\widetilde{E}}_{BC}(z,\vec{r},\omega) = \frac{i\omega e}{c^2 z} \int_{z_B}^{z_C} dz' \exp\left[i\Phi_{BC}\right] \left(\theta_x \vec{x} + \theta_y \vec{y}\right) \tag{49}$$

where

$$\Phi_{BC} = \frac{\omega}{c}\left[\frac{\theta^2}{2} z + \frac{z'}{2}\left(\frac{1}{\bar{\gamma}_z^2} + \theta^2\right)\right] . \tag{50}$$

6.1.2 *Field contribution calculated along the straight sections*

With the help of Eq. (13) we write the contribution from the straight line AB as

$$\vec{\vec{E}}_{AB} = \frac{i\omega e}{c^2 z} \int\limits_{z_A}^{z_B} dz' \exp\left[i\Phi_{AB}\right] \left(\theta_x \vec{x} + \theta_y \vec{y}\right) \tag{51}$$

where Φ_{AB} in Eq. (51) is given by

$$\Phi_{AB} = \frac{\omega}{c}\left[\frac{\theta^2}{2} z + \frac{z'}{2}\left(\frac{1}{\gamma^2} + \theta^2\right) - \frac{L_w}{4\bar{\gamma}_z^2} + \frac{L_w}{4\gamma^2}\right] . \tag{52}$$

The contribution from the straight section CD is similar to that from the straight section AB and reads

$$\vec{\vec{E}}_{CD} = \frac{i\omega e}{c^2 z} \int\limits_{z_C}^{z_D} dz' \exp\left[i\Phi_{CD}\right] \left(\theta_x \vec{x} + \theta_y \vec{y}\right) , \tag{53}$$

where Φ_{CD} in Eq. (53) is given by

$$\Phi_{CD} = \frac{\omega}{c}\left[\frac{\theta^2}{2} z + \frac{z'}{2}\left(\frac{1}{\gamma^2} + \theta^2\right) + \frac{L_w}{4\bar{\gamma}_z^2} - \frac{L_w}{4\gamma^2}\right] . \tag{54}$$

In general, the phases Φ_{CD} and Φ_{AB} start exhibiting oscillatory behavior when $z'/(2\gamma^2 \bar{\lambda}) \sim 1$, which gives a maximal integration range in the longitudinal direction. Similarly as before, in general one has that the formation lengths L_{fs1} and L_{fs2} for the straight sections AB and CD can be written as $L_{\mathrm{fs}(1,2)} \sim \min\left[\bar{\lambda}\gamma^2, L_{(1,2)}\right]$.

6.1.3 *Total field and energy spectrum of radiation*

The contributions for segment AB and segment CD are given by Eq. (51) and Eq. (53). One obtains

$$
\begin{aligned}
\vec{\widetilde{E}}_{AB} = & \frac{i\omega e L_1}{c^2 z}\exp\left[\frac{i\omega\theta^2 z}{2c}\right]\vec{\theta}\,\mathrm{sinc}\left[\frac{\omega L_1}{4c}\left(\frac{1}{\gamma^2}+\theta^2\right)\right] \\
& \times\exp\left[-\frac{i\omega L_w}{4c}\left(\frac{1}{\bar{\gamma}_z^2}+\theta^2\right)\right]\exp\left[-\frac{i\omega L_1}{4c}\left(\frac{1}{\gamma^2}+\theta^2\right)\right] .
\end{aligned}
\tag{55}
$$

Similarly,

$$
\begin{aligned}
\vec{\widetilde{E}}_{CD} = & \frac{i\omega e L_2}{c^2 z}\exp\left[\frac{i\omega\theta^2 z}{2c}\right]\vec{\theta}\,\mathrm{sinc}\left[\frac{\omega L_2}{4c}\left(\frac{1}{\gamma^2}+\theta^2\right)\right] \\
& \times\exp\left[\frac{i\omega L_w}{4c}\left(\frac{1}{\bar{\gamma}_z^2}+\theta^2\right)\right]\exp\left[\frac{i\omega L_2}{4c}\left(\frac{1}{\gamma^2}+\theta^2\right)\right] .
\end{aligned}
\tag{56}
$$

Finally, the contribution for the segment BC is obtained from Eq. (49). Calculations yield:

$$
\vec{\widetilde{E}}_{BC} = \frac{i\omega e L_w}{c^2 z}\exp\left[\frac{i\omega\theta^2 z}{2c}\right]\vec{\theta}\,\mathrm{sinc}\left[\frac{\omega L_w}{4c}\left(\frac{1}{\bar{\gamma}_z^2}+\theta^2\right)\right] .
\tag{57}
$$

The total field produced by the setup is obtained by summing up Eq. (55), Eq. (56) and Eq. (57). By this, we are neglecting bending magnet contributions. A sufficient condition (in addition to the already accepted ones, $N_w \gg 1$ and $\lambda\!\!\!^{-}/\lambda\!\!\!^{-}_r \gg 1$) is $\lambda\!\!\!^{-} \gg R/\bar{\gamma}_z^3$. In fact, we may neglect bending magnet contributions for $\delta_{1,2} \ll 1$, but in this setup $L_{1,2}$ may be set to zero, in which case we should also impose that the formation length of the bend be much shorter than $\bar{\gamma}_z^2 \lambda\!\!\!^{-}$, which reduces to $\lambda\!\!\!^{-} \gg R/\bar{\gamma}_z^3$.

As before, the observation angle is measured starting from the center of the undulator, located at $z = 0$, i.e. $\vec{\theta} = \vec{r}/z$. The spectral energy density per unit angle can be written substituting the resultant total field in Eq. (24). We obtain

$$
\frac{dW}{d\omega d\Omega} = \frac{e^2}{\pi^2 c}\frac{\gamma^4\theta^2}{(1+\gamma^2\theta^2)^2}\Bigg| - \exp\left[-i\frac{\omega L_w}{4c\gamma^2}\left(1+\frac{K^2}{2}+\gamma^2\theta^2\right)\right]
$$

$$
\begin{aligned}
&+\exp\left[-i\frac{\omega L_1}{2c\gamma^2}\left(1+\gamma^2\theta^2\right)-i\frac{\omega L_w}{4c\gamma^2}\left(1+\frac{K^2}{2}+\gamma^2\theta^2\right)\right]\\
&+\frac{1/\gamma^2+\theta^2}{1/\bar{\gamma}_z^2+\theta^2}\left\{-\exp\left[\frac{i\omega L_w}{4c\gamma^2}\left(1+\frac{K^2}{2}+\gamma^2\theta^2\right)\right]\right.\\
&\left.+\exp\left[-\frac{i\omega L_w}{4c\gamma^2}\left(1+\frac{K^2}{2}+\gamma^2\theta^2\right)\right]\right\}+\exp\left[i\frac{\omega L_w}{4c\gamma^2}\left(1+\frac{K^2}{2}+\gamma^2\theta^2\right)\right]\\
&-\exp\left[i\frac{\omega L_2}{2c\gamma^2}\left(1+\gamma^2\theta^2\right)+\frac{i\omega L_w}{4c\gamma^2}\left(1+\frac{K^2}{2}+\gamma^2\theta^2\right)\right]\Bigg|^2, \qquad (58)
\end{aligned}
$$

that is equivalent to the analogous expression in [9].

Note that L_1, L_2 and L_w can assume different values. γ and $\bar{\gamma}_z$ are also different. It may therefore seem convenient to introduce different normalized quantities, referring to the undulator and the straight lines. However, in the end we are interested in summing up all contributions from different sources, so that it is important to keep a common definition of vertical displacement (or observation angle). Therefore we prescribe the same normalization for all quantities:

$$
\hat{\vec{\theta}}=\sqrt{\frac{L_{\mathrm{tot}}}{\bar{\lambda}}}\vec{\theta}\,,\phi_t=\frac{L_{\mathrm{tot}}}{\gamma^2\bar{\lambda}}\quad\text{and}\quad\hat{\vec{r}}=\frac{\vec{r}}{\sqrt{L_{\mathrm{tot}}\bar{\lambda}}}\,. \qquad (59)
$$

Then, we introduce parameters $\hat{L}_1 = L_1/L_{\mathrm{tot}}$, $\hat{L}_2 = L_2/L_{\mathrm{tot}}$, $\hat{L}_w = L_w/L_{\mathrm{tot}}$, $\phi_{1,2} = L_{1,2}/(\gamma^2\bar{\lambda}) = \hat{L}_{1,2}\phi_t$ and $\phi_w = L_w/(\bar{\gamma}_z^2\bar{\lambda})$, as seen above. Here it should be clear that ϕ_t has been introduced only for notational convenience, while real parameters related to the physics of the problem are $\phi_{1,2}$. Finally, we define $\hat{z}_s = z_s/L_{\mathrm{tot}}$. From Eq. (58) follows

$$
\begin{aligned}
\hat{z}^2\hat{I}=&\frac{4\hat{\theta}^2}{(\phi_t+\hat{\theta}^2)^2}\Bigg|\exp\left[-\frac{i\hat{L}_1}{2}\left(\phi_t+\hat{\theta}^2\right)-\frac{i}{4}\left(\phi_w+\hat{L}_w\hat{\theta}^2\right)\right]-\exp\left[-\frac{i}{4}\left(\phi_w+\hat{L}_w\hat{\theta}^2\right)\right]\\
&+\frac{\phi_t+\hat{\theta}^2}{\phi_w/\hat{L}_w+\hat{\theta}^2}\left\{-\exp\left[\frac{i}{4}\left(\phi_w+\hat{L}_w\hat{\theta}^2\right)\right]+\exp\left[-\frac{i}{4}\left(\phi_w+\hat{L}_w\hat{\theta}^2\right)\right]\right\}\\
&-\exp\left[\frac{i\hat{L}_2}{2}\left(\phi_t+\hat{\theta}^2\right)+\frac{i}{4}\left(\phi_w+\hat{L}_w\hat{\theta}^2\right)\right]+\exp\left[\frac{i}{4}\left(\phi_w+\hat{L}_w\hat{\theta}^2\right)\right]\Bigg|^2, \qquad (60)
\end{aligned}
$$

where $\hat{I} = \left|\vec{\hat{E}}\right|^2$ and $\vec{\hat{E}} \equiv \vec{\bar{E}}\sqrt{\bar{\lambda} L_{\mathrm{tot}}}\; c/e$. Note that outside the undulator the longitudinal velocity is nearer to c than inside ($\bar{\gamma}_z^2 < \gamma^2$). It follows that the contribution of the undulator is suppressed compared with that of the straight sections, and in the case of comparable lengths and $K^2 \gg 1$, the straight section contribution becomes dominant.

In the special case for $\hat{L}_1 = \hat{L}_2 = \hat{L}_w \equiv \hat{L}/3$, $\phi_{1,2} = \phi_t/3$, and Eq. (60) simplifies to

$$\begin{aligned}\hat{z}^2\hat{I} = \frac{4\hat{\theta}^2}{(\phi_t + \hat{\theta}^2)^2}\Bigg| & -4i\cos\left[\frac{\hat{L}}{12}\left(2\hat{\theta}^2 + \phi_t\right) + \frac{\phi_w}{4}\right]\sin\left[\frac{\hat{L}}{12}\left(\hat{\theta}^2 + \phi_t\right)\right] \\ & -2i\frac{\phi_t + \hat{\theta}^2}{3\phi_w/\hat{L} + \hat{\theta}^2}\sin\left[\frac{1}{12}\left(3\phi_w + \hat{L}\hat{\theta}^2\right)\right]\Bigg|^2 . \end{aligned} \tag{61}$$

Eq. (61) can be readily evaluated. As an example, we can calculate the intensity distribution of TUR emitted by the SASE 1 European XFEL setup at a wavelength $\lambda = 400$ nm. We assume that the XFEL operates at 17.5 GeV. Setup parameters are $L_1 = L_w = L_2 = 200$ m, $R = 400$ m, $K = 3.3$ and $\lambda_w = 3.56$ cm [22]. In this case $\delta \sim 10^{-3}$ and $\delta_w \sim 1/N_w \sim 10^{-4}$, while $\phi_t \simeq 8.0$ and $\phi_w \simeq 52$. Results are plotted in Fig. 15. In that figure, we also propose a comparison with outcomes from SRW at $z = 6000$ m (vertical and horizontal cuts).

In the far zone, well-accepted expressions for the TUR emission are reported in literature [17, 18, 19, 21], that are equivalent to the following equation for the radiation energy density as a function of angle and frequency:

$$\frac{dW}{d\omega d\Omega} = \frac{e^2}{\pi^2 c}\left[\frac{\gamma^2\theta K^2}{(1 + K^2/2 + \gamma^2\theta^2)(1 + \gamma^2\theta^2)}\right]^2 \sin^2\left[\frac{\pi L_w}{2\gamma^2\lambda}\left(1 + \frac{K^2}{2} + \gamma^2\theta^2\right)\right]. \tag{62}$$

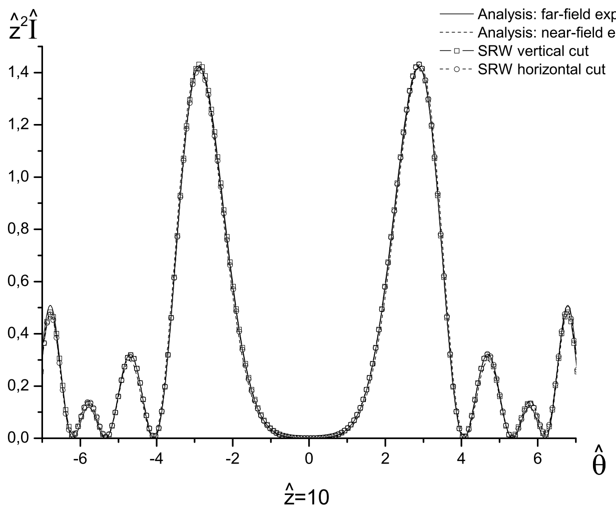

Fig. 15. Cross-check of Eq. (61) with the help of SRW. Here $L_1 = L_w = L_2 = 200$ m, $E = 17.5$ GeV, $\lambda = 400$ nm, $R = 400$ m, and $K = 3.3$. Here $\lambda_w = 3.56$ cm. The observer is located at $z = 6000$ m. Circles represent horizontal and vertical cuts of the intensity profiles calculated numerically with SRW. The solid curve is calculated with Eq. (61). The dashed curve is obtained with the near-zone expressions Eqs. (69)-(72).

We will show that Eq. (62) cannot be applied for TUR calculations. In our understanding, there cannot be any range of parameters in the setup in Fig. 14 where Eq. (62) is valid.

In order to prove this it is sufficient to compare Eq. (62) with Eq. (58). Eq. (62) does not depend on the straight section lengths L_1 or L_2, and can be applied when $L_1,\ L_2 \longrightarrow 0$.

However, in that limit, Eq. (58) reduces to:

$$\frac{dW}{d\omega d\Omega} = \frac{e^2}{\pi^2 c}\left[\frac{2\gamma^2\theta}{1+K^2/2+\gamma^2\theta^2}\right]^2 \sin^2\left[\frac{\pi L_w}{2\gamma^2\lambda}\left(1+\frac{K^2}{2}+\gamma^2\theta^2\right)\right] , \qquad (63)$$

that is obviously different from Eq. (62). Also note that in the limit for $K \longrightarrow 0$

Eq. (62) tends to zero, whereas Eq. (63) gives back Eq. (25) as it must be.

6.2 *Virtual source characterization and field propagation*

There is a general need, in the FEL community, to extend the current theory of TUR to cover the near zone. For instance, a possible use of coherent TUR to produce visible light synchronized with X-rays from an X-ray free-electron laser is discussed in [25]. As we have seen, TUR can be discussed as a more complicated edge-radiation setup. Within the sharp-edge approximation we have contributions from three parts, two straight lines and the undulator. The undulator contribution is similar to a straight line contribution, the only difference being a different average longitudinal velocity of the electron. Then, the far-zone region can be identified by distances $z \gg L_{tot}$.

Expressions in Eq. (55), Eq. (56) and Eq. (57) can be interpreted as far field radiation from separate virtual sources. For each far field contribution we use a picture with two virtual sources, located at the ends of the straight sections and of the undulator. This makes a total of six sources. However, since the virtual source at the downstream [upstream] edge of the first [second] straight section has the same longitudinal position of the virtual source at the upstream [downstream] edge of the undulator, i.e. $z = -L_w/2$ [$z = L_w/2$], we combine them together, summing them up by superposition principle. As a result, we are left with only four sources, located at

$$z_{s1} = -\frac{L_w}{2} - L_1 \ , \quad z_{s2} = -\frac{L_w}{2} \ , \quad z_{s3} = \frac{L_w}{2} \ , \quad \text{and} \quad z_{s4} = \frac{L_w}{2} + L_2 \ . \qquad (64)$$

We obtain an explicit expression for these sources with the help of Eq. (55), Eq. (56) and Eq. (57), proceeding analogously as in Section 5.2:

$$\vec{\widetilde{E}}_{s1}\left(-\frac{L_w}{2}-L_1,\vec{r}\right)=\frac{2\omega e}{c^2\gamma}\exp\left[-\frac{i\omega L_1}{2c\gamma^2}\right]\exp\left[-\frac{i\omega L_w}{4c\gamma_z^2}\right]\frac{\vec{r}}{r}K_1\left(\frac{\omega r}{c\gamma}\right)\ , \tag{65}$$

$$\begin{aligned}\vec{\widetilde{E}}_{s2}\left(-\frac{L_w}{2},\vec{r}\right)=&-\frac{2\omega e}{c^2\gamma}\exp\left[-\frac{i\omega L_w}{4c\gamma_z^2}\right]\frac{\vec{r}}{r}K_1\left(\frac{\omega r}{c\gamma}\right)\\&+\frac{2\omega e}{c^2\gamma_z}\exp\left[-\frac{i\omega L_w}{4c\gamma_z^2}\right]\frac{\vec{r}}{r}K_1\left(\frac{\omega r}{c\gamma_z}\right)\ ,\end{aligned} \tag{66}$$

$$\begin{aligned}\vec{\widetilde{E}}_{s3}\left(\frac{L_w}{2},\vec{r}\right)=&-\frac{2\omega e}{c^2\gamma_z}\exp\left[\frac{i\omega L_w}{4c\gamma_z^2}\right]\frac{\vec{r}}{r}K_1\left(\frac{\omega r}{c\gamma_z}\right)\\&+\frac{2\omega e}{c^2\gamma}\exp\left[\frac{i\omega L_w}{4c\gamma_z^2}\right]\frac{\vec{r}}{r}K_1\left(\frac{\omega r}{c\gamma}\right)\ ,\end{aligned} \tag{67}$$

$$\vec{\widetilde{E}}_{s4}\left(\frac{L_w}{2}+L_2,\vec{r}\right)=-\frac{2\omega e}{c^2\gamma}\exp\left[\frac{i\omega L_2}{2c\gamma^2}\right]\exp\left[\frac{i\omega L_w}{4c\gamma_z^2}\right]\frac{\vec{r}}{r}K_1\left(\frac{\omega r}{c\gamma}\right)\ . \tag{68}$$

In order to calculate the field at any distance z we proceed in analogy with Eq. (40), applying the propagation formula Eq. (14). As before, the above given equations for the sources can also be used as input to any Fourier code to calculate the field evolution in the presence of whatever optical beamline. However, here we restrict ourselves to the free-space case. In order to simplify the presentation of the electric field we take advantage of polar coordinates and we use the definition $\vec{\hat{E}} \equiv \vec{\widetilde{E}}\sqrt{\lambdabar L_{\mathrm{tot}}}\ c/e$ (so that $\hat{I}$, introduced in Eq. (26), is given by $\hat{I} = |\vec{\hat{E}}|^2$) for the field in normalized units. Note that here $\hat{z} = z/L_{\mathrm{tot}}$. We obtain four field contributions, one for each source:

$$\begin{aligned}\vec{\hat{E}}_1\left(\hat{z},\vec{\hat{\theta}}\right)=&-\left\{\frac{\vec{\hat{\theta}}}{\hat{\theta}}\frac{2\sqrt{\phi_t}\exp[-i\hat{L}_1\phi_t/2]\exp\left[-i\phi_w/4\right]}{\hat{z}+\hat{L}_w/2+\hat{L}_1}\right.\\&\times\int_0^{\infty}d\hat{r}'\hat{r}'K_1\left(\sqrt{\phi_t}\hat{r}'\right)J_1\left(\frac{\hat{\theta}\hat{r}'\hat{z}}{\hat{z}+\hat{L}_w/2+\hat{L}_1}\right)\end{aligned}$$

$$\times \exp\left[\frac{i\hat{r}'^2}{2\left(\hat{z}+\hat{L}_w/2+\hat{L}_1\right)}\right]\exp\left[\frac{i\hat{\theta}^2\hat{z}^2}{2\left(\hat{z}+\hat{L}_w/2+\hat{L}_1\right)}\right]\Bigg\} \ . \tag{69}$$

$$\begin{aligned}
\vec{\hat{E}}_2\left(\hat{z},\vec{\hat{\theta}}\right) = & \left\{\frac{\vec{\hat{\theta}}}{\hat{\theta}}\frac{2\sqrt{\phi_t}\exp\left[-i\phi_w/4\right]}{\hat{z}+\hat{L}_w/2}\exp\left[\frac{i\hat{\theta}^2\hat{z}^2}{2\left(\hat{z}+\hat{L}_w/2\right)}\right]\right. \\
& \left.\times\int_0^\infty d\hat{r}'\,\hat{r}' K_1\left(\sqrt{\phi_t}\hat{r}'\right) J_1\left(\frac{\hat{\theta}\hat{r}'\hat{z}}{\hat{z}+\hat{L}_w/2}\right)\exp\left[\frac{i\hat{r}'^2}{2\left(\hat{z}+\hat{L}_w/2\right)}\right]\right\} \\
& -\left\{\frac{\vec{\hat{\theta}}}{\hat{\theta}}\frac{2\sqrt{\phi_w/\hat{L}_w}\exp\left[-i\phi_w/4\right]}{\hat{z}+\hat{L}_w/2}\exp\left[\frac{i\hat{\theta}^2\hat{z}^2}{2\left(\hat{z}+\hat{L}_w/2\right)}\right]\right. \\
& \left.\times\int_0^\infty d\hat{r}'\,\hat{r}' K_1\left(\sqrt{\phi_w/\hat{L}_w}\hat{r}'\right) J_1\left(\frac{\hat{\theta}\hat{r}'\hat{z}}{\hat{z}+\hat{L}_w/2}\right)\exp\left[\frac{i\hat{r}'^2}{2\left(\hat{z}+\hat{L}_w/2\right)}\right]\right\}
\end{aligned} \tag{70}$$

$$\begin{aligned}
\vec{\hat{E}}_3\left(\hat{z},\vec{\hat{\theta}}\right) = & -\left\{\frac{\vec{\hat{\theta}}}{\hat{\theta}}\frac{2\sqrt{\phi_t}\exp\left[i\phi_w/4\right]}{\hat{z}-\hat{L}_w/2}\exp\left[\frac{i\hat{\theta}^2\hat{z}^2}{2\left(\hat{z}-\hat{L}_w/2\right)}\right]\right. \\
& \left.\times\int_0^\infty d\hat{r}'\,\hat{r}' K_1\left(\sqrt{\phi_t}\hat{r}'\right) J_1\left(\frac{\hat{\theta}\hat{r}'\hat{z}}{\hat{z}-\hat{L}_w/2}\right)\exp\left[\frac{i\hat{r}'^2}{2\left(\hat{z}-\hat{L}_w/2\right)}\right]\right\} \\
& +\left\{\frac{\vec{\hat{\theta}}}{\hat{\theta}}\frac{2\sqrt{\phi_w/\hat{L}_w}\exp\left[i\phi_w/4\right]}{\hat{z}-\hat{L}_w/2}\exp\left[\frac{i\hat{\theta}^2\hat{z}^2}{2\left(\hat{z}-\hat{L}_w/2\right)}\right]\right. \\
& \left.\times\int_0^\infty d\hat{r}'\,\hat{r}' K_1\left(\sqrt{\phi_w/\hat{L}_w}\hat{r}'\right) J_1\left(\frac{\hat{\theta}\hat{r}'\hat{z}}{\hat{z}-\hat{L}_w/2}\right)\exp\left[\frac{i\hat{r}'^2}{2\left(\hat{z}-\hat{L}_w/2\right)}\right]\right\}
\end{aligned} \tag{71}$$

$$\begin{aligned}
\vec{\hat{E}}_4\left(\hat{z},\vec{\hat{\theta}}\right) = & \left\{\frac{\vec{\hat{\theta}}}{\hat{\theta}}\frac{2\sqrt{\phi_t}\exp\left[i\hat{L}_2\phi_t/2\right]\exp\left[i\phi_w/4\right]}{\hat{z}-\hat{L}_w/2-\hat{L}_2}\right. \\
& \times\int_0^\infty d\hat{r}'\,\hat{r}' K_1\left(\sqrt{\phi_t}\hat{r}'\right) J_1\left(\frac{\hat{\theta}\hat{r}'\hat{z}}{\hat{z}-\hat{L}_w/2-\hat{L}_2}\right) \\
& \left.\times\exp\left[\frac{i\hat{r}'^2}{2\left(\hat{z}-\hat{L}_w/2-\hat{L}_2\right)}\right]\exp\left[\frac{i\hat{\theta}^2\hat{z}^2}{2\left(\hat{z}-\hat{L}_w/2-\hat{L}_2\right)}\right]\right\} \ .
\end{aligned} \tag{72}$$

Eqs. (69) to (72) can be used to calculate the field, and hence the intensity, at any position of interest in the far and in the near zone. Obviously, in the far zone, for $\hat{z} \gg 1$, the square modulus of their sum reduces to Eq. (61). As before, It is interesting to cross-check Eqs. (69) to (72) with the computer code SRW. We used the same numerical parameters as before: $L_1 = L_w = L_2 = 200$ m, $E = 17.5$ GeV, $\lambda = 400$ nm and $R = 400$ m, with an undulator parameter $K = 3.3$. Additionally, we chose different values $z = 360$m, $z = 600$m, $z = 1200$m (see Figs. 16 ÷ 18), and $z = 6000$m (see Fig. 15), corresponding to $\hat{z} = 0.6$, $\hat{z} = 1.0$, $\hat{z} = 1.5$, $\hat{z} = 2.0$ and $\hat{z} = 10$ (which is the far-zone case treated before). Here the bending plane is the horizontal plane. As the observation point becomes nearer to the edge of the magnet, the influence of the bending magnet becomes more and more important, an effect which is evident in the figures from the horizontal cuts of SRW two-dimensional intensity profiles. From Figs. 15÷18 we can see that the analytical result for the vertical cut is valid with good accuracy up to $\hat{z} = 0.6$.

7 Conclusions

In this article we showed how the theory of laser beams can be used to characterize radiation field associated with any Edge Radiation (ER) setup. In fact, in the space-frequency domain, ER beams could be described in terms of laser-like beams, with large transverse dimensions compared to the wavelength. Similarly to usual laser beams, ER beams were shown to exhibit a virtual "waist" with a plane wavefront. The field distribution of ER across the waist turned out to be strictly related to the inverse Fourier

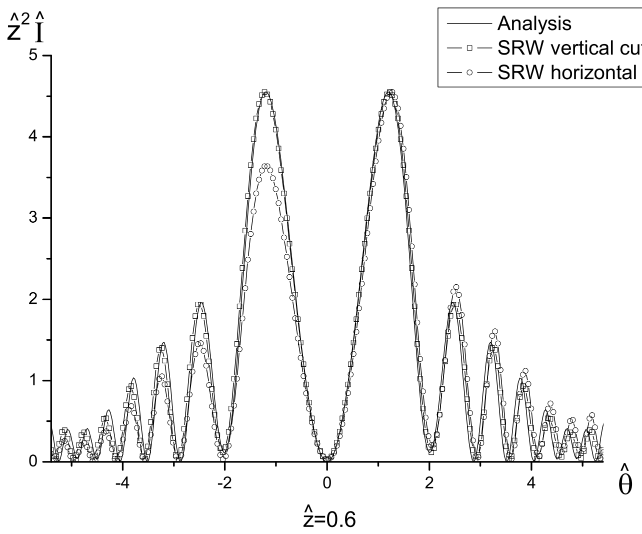

Fig. 16. Cross-check of analytical results with SRW. Here $L_1 = L_w = L_2 = 200$ m, $E = 17.5$ GeV, $\lambda = 400$ nm, $R = 400$ m, and $K = 3.3$. The observer is located at $z = 360$ m. Here $\lambda_w = 3.56$ cm. Horizontal and vertical cuts of the intensity profiles are compared with results obtained with the help of Eqs. (69) to (72).

transform of the angular field-distribution in the far-zone. As a result, standard Fourier Optics techniques could be taken advantage of, and the field could be propagated to characterize ER beams at any position down the beamline. In particular, we reconstructed the near-field distribution from the knowledge of the far-field ER pattern. This could be accomplished by (i) describing the far-field pattern with known analytical formulas, (ii) finding the virtual source(s) and (iii) propagating the virtual source distribution in the near (and far) zone.

After a qualitative discussion in Section 2, we applied our techniques to a typical setup constituted by a straight section between bends in Sections 3, 4 and 5. These Sections constitute the first comprehensive treatment of ER, in the sense that we consistently used similarity techniques for the first time,

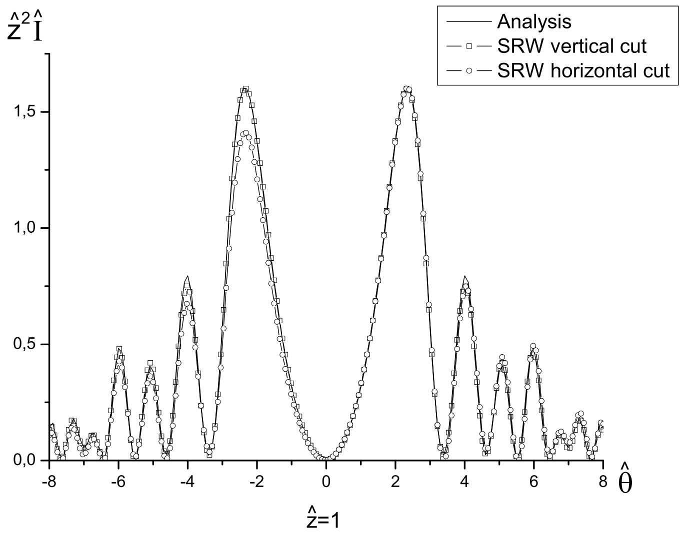

Fig. 17. Cross-check of analytical results with SRW. Here $L_1 = L_w = L_2 = 200$ m, $E = 17.5$ GeV, $\lambda = 400$ nm, $R = 400$ m, and $K = 3.3$. Here $\lambda_w = 3.56$ cm. The observer is located at $z = 600$ m. Horizontal and vertical cuts of the intensity profiles are compared with results obtained with the help of Eqs. (69) to (72).

allowing discussion and physical understanding of many asymptotes of the parameter space together with their region of applicability. In particular, the main parameters of the theory are found to be δ, the ratio between the bends formation length and the straight section length, and ϕ, the ratio between the length of the straight section and the maximal formation length of ER. Note that introduction of the parameter δ allowed us to define for the first time "how sharp" the edges are, and to specify the region of applicability of ER theory. A classification of regions of observation of interest, which is regarded by us as a novel result, is presented in Section 5.3 with the help of dimensionless parameters.

In Section 6 we applied our treatment to deal with a Transition Undulator Radiation (TUR) setup. As before, we relied on virtual source expressions

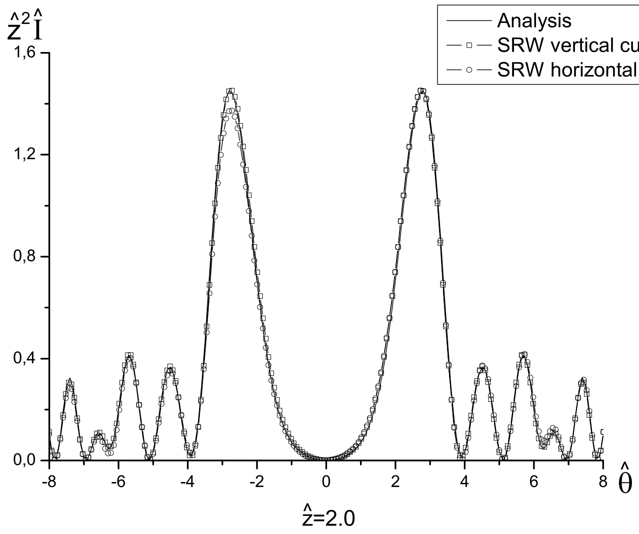

Fig. 18. Cross-check of analytical results with SRW. Here $L_1 = L_w = L_2 = 200$ m, $E = 17.5$ GeV, $\lambda = 400$ nm, $R = 400$ m, and $K = 3.3$. Here $\lambda_w = 3.56$ cm. The observer is located at $z = 1200$ m. Horizontal and vertical cuts of the intensity profiles are compared with results obtained with the help of Eqs. (69) to (72).

derived from the far-field pattern. These virtual sources were propagated in free-space in the near zone, thus providing for the first time an exact analytical characterization of TUR in the near zone.

As a final remark, it should be noted that in our work we consistently exploited both theoretical and numerical results from simulation. These approaches are complementary, and we first took advantage of such complementarity. Computer codes can easily account for finite bending magnet edge length (finite value of δ) in a particular set of problem parameters. From this viewpoint, our theory can be used to prepare, based on similarity techniques, particular sets of problem parameters to be used as input for computer codes, which subsequently return universal plots presenting the accuracy of ER theory in terms of dimensionless parameters.

Acknowledgements

We thank our DESY collegues Martin Dohlus, Michael Gensch and Petr Ilinski for many useful discussions, Massimo Altarelli , Reinhard Brinkmann and Edgar Weckert for their interest in this work.

References

[1] M.M. Nikitin, A.F. Medvedyev, M.B. Moiseyev, and V. Ya. Epp, Sov. Phys. JETP 52 (1980) 388.

[2] M.M. Nikitin, A.F. Medvedyev and M.B. Moiseyev, IEEE Trans. Nucl. Sci. NS-28 3 (1981) 3130.

[3] E.G. Bessonov, Sov. Phys. Tech. Phys. 28 (1983) 837.

[4] Yu. A. Bashmakov, Rev. Sci. Instrum 63 (1992) 343.

[5] O.V. Chubar and N.V. Smolyakov, J. Optics (Paris) 24 (1993) 117.

[6] O.V. Chubar and N.V. Smolyakov, Proc. of PAC93 (1993) 1626.

[7] R.A. Bosch et al., Rev. Sci. Instrum. 67 (1995) 3346.

[8] R.A. Bosch and O.V. Chubar, Proc. of SRI'97, AIP Conf. Proc. 417, edited by E. Fontes (AIP, Woodbury, NY), 1997, pp. 35 41.

[9] R.A. Bosch, Il Nuovo Cimento 20 4 (1998) 483 .

[10] R.A. Bosch, Nucl. Instr. Meth. Phys. Res. A 431 (1999) 320.

[11] Y.-L. Mathis et al. Phys. Rev. Lett. 80 (1998) 1220.

[12] P. Roy, J-B. Brubach et al., Nucl. Instr. Meth. Phys. Res. A 467 (2001) 426.

[13] R.A. Bosch, R.A. Bosch, Nucl. Instr. Meth. Phys. Res. A 492 (2002) 284.

[14] R.A. Bosch, Nucl. Instr. Meth. Phys. Res. A 482 (2002) 789.

[15] P. Dumas and M. J. Tobin, Spectroscopy Europe 15, 17 (2003)

[16] G. Geloni, E. Saldin, E. Schneidmiller and M. Yurkov, Optics Communications 276 (2007) 167.

[17] K.-J. Kim, Phys. Rev. Lett. 76 (1996) 1244.

[18] B.M. Kincaid, Il Nuovo Cimento Soc. Ital. Fis 20D (1998) 495.

[19] M. Castellano, Nucl. Instr and Meth. in Phys. Res. A 391 (1997) 375.

[20] R.A. Bosch, Nucl. Instr. Meth. Phys. Res. A 386 (1997) 525.

[21] P. Roy et al. Phys. Rev. Lett. 84 (2000) 3.

[22] M. Altarelli et al. (Eds.), XFEL: The European X-Ray Free-Electron Laser. Technical Design Report, DESY 2006-097, Hamburg, 2006 (See also http://xfel.desy.de).

[23] J. Arthur et al. Linac Coherent Light Source (LCLS). Conceptual Design Report, SLAC-R593, Stanford, USA, 2002 (See also http://www-ssrl.slac.stanford.edu/lcls/cdr).

[24] Tanaka, T. & Shintake, T. (Eds.): SCSS X-FEL Conceptual Design Report. Riken Harima Institute, Hyogo, Japan, 2005 (see also http://www-xfel.spring8.or.jp).

[25] G. Geloni, E. Saldin, E. Schneidmiller and M. Yurkov, Opt. Commun. 281 (2008) 3762.

[26] O. Chubar, P.Elleaume and A. Snigirev , Nucl. Instr. Meth. Phys. Res. A 435 (1999) 495.

[27] K.-J. Kim, Characteristics of Synchrotron Radiation, in Phys. of Part. Acc. 184, AIP Conf. Proc., Am. Inst. of Phys., New York, 1984.

[28] G. P. Williams, Rep. Prog. Phys. 69 (2006) 301.

[29] Y. Takayama and S. Kamada, Phys. Rev. E 59 (1999) 7128.

[30] G. Geloni, E. Saldin, E. Schneidmiller and M. Yurkov, Fourier Optics Treatment of Classical Relativistic Electrodynamics, DESY 06-127, 2006.

[31] R. A. Bosch, Phys. Rev. ST AB 10 (2007) 050701.

Figure Captions

Fig. 1. Four main types of edge radiation setups: (a) Far-infrared beamline for synchrotron radiation source using edge radiation. (b) Arrival-time monitor for XFEL source using optical coherent edge radiation. (c) Electron bunch length monitor for XFEL using far-infrared coherent edge radiation. (d) Ultra-short electron bunch diagnostic for laser-plasma accelerator facility using optical coherent edge radiation.

Fig. 2. Illustrative calculations of the effect of bending magnet separation on the directivity diagram of the radiation. The bending magnet radius $R = 400$ m, the relativistic factor $\gamma = 3.42 \cdot 10^4$, and the wavelength of interested $\lambda = 400$ nm are fixed, while the straight section length varies from $L = 0$ up to $L \gg \gamma^2 \bar{\lambda} \simeq 100$ m. In this setup (as well as in all others in this paper) $\lambda \gg \lambda_c \simeq 0.1$Å. Case (a) is a bending magnet setup. Case (b) is a complex setup, where the radiation beam divergence is practically the same as in (a). Case (c) illustrates an ER setup. Bending magnet separation dramatically lowers the radiation beam divergence. (d) Optimal bending magnet separation. The straight section length $L \simeq \gamma^2 \bar{\lambda}$ corresponds to a radiation beam divergence $\theta \simeq 1/\gamma$. (e) Further increase of L only leads to the appearance of finer structures in the radiation profile. 2D plots on the left show the spectral energy density per unit angle as a function of the horizontal and vertical angles θ_x and θ_y for various lengths of the straight section. Middle plots are obtained cutting the 2D spectral energy density profile at $x = 0$. Right plots show a schematic of the considered layout.

Fig. 3. Verification of similarity techniques. Left and right plots show the

normalized spectral energy density per unit angle as a function of the horizontal and vertical angles $\hat{\theta}_x$ and $\hat{\theta}_y$ respectively (at $\hat{\theta}_y = 0$ and $\hat{\theta}_x = 0$ respectively). (a) Case $\delta \simeq 0.43$ and $\phi \simeq 6.7 \cdot 10^{-3}$. Solid curve is the result of SRW calculations with $L = 0.5$ m, $R = 400$ m, $\lambda = 400$ nm at 17.5 GeV. Dotted curve is the result for $L = 1$ m, $R = 800$ m, $\lambda = 800$ nm at 17.5 GeV. (b) Case $\delta \ll 1$ and $\phi \simeq 4$. Solid curve is the result of SRW calculations with $L = 300$ m, $R = 400$ m, $\lambda = 400$ nm, at 17.5 GeV (corresponding to $\delta \simeq 7 \cdot 10^{-4}$). Dotted curve is the result for $L = 150$ m, $R = 400$ m, $\lambda = 800$ nm at 8.5 GeV (corresponding to $\delta \simeq 2 \cdot 10^{-3}$).

Fig. 4. Illustration of self-similarity techniques. Left and right plots show the normalized spectral energy density per unit angle as a function of the horizontal and vertical angles $\hat{\theta}_x$ and $\hat{\theta}_y$ respectively (at $\hat{\theta}_y = 0$ and $\hat{\theta}_x = 0$ respectively). The profile of the spectral energy density per unit angle asymptotically approaches the self-similar form $I/I_{\max} = F(\hat{\theta}_x, \hat{\theta}_y)$ for $\delta \ll 1$ and $\phi \ll 1$. Solid curve is the result of SRW calculations with $\delta \simeq 0.02$ and $\phi \simeq 0.13$. Dotted curve is refers to the case $\delta = 0.01$ and $\phi = 0.27$ instead.

Fig. 5. Geometry for SR from a bending magnet.

Fig. 6. Normalized spectral energy density per unit angle of the radiation from the setup in Fig. 1(a) for different values of ϕ.

Fig. 7. Spectral energy density per unit angle as a function of the normalized angle $\hat{\theta}$ for two different edge length parameters $\delta = 0.2$ and $\delta = 0.02$. Here the straight section length parameter $\phi \simeq 0.01$. Left and right plots are obtained cutting the profile of the spectral energy density per unit angle at $\hat{\theta}_y = 0$ and $\hat{\theta}_x = 0$ respectively (i.e. electron motion is in xz plane). The dotted curves are calculated with the analytical formula Eq. (27). Solid lines

are the results of numerical calculations with computer code SRW.

Fig. 8. Spectral energy density per unit angle as a function of the normalized angle $\hat{\theta}$ for different straight-section length parameters ϕ calculated after Eq. (27) and comparison with the asymptotic limit for $\phi \ll 1$ in Eq. (28).

Fig. 9. Normalized spectral energy density at the virtual source, $\hat{I}_s$, as a function of $\hat{r}$ (upper plot) and 3D view as a function of $\hat{x}$ and $\hat{y}$.

Fig. 10. Evolution of $\hat{z}^2\hat{I}$ for edge radiation in the limit for $\phi \ll 1$. These profiles, calculated with Eq. (34), are shown as a function of angles at different observation distances $\hat{z} = 0.6$, $\hat{z} = 1.0$, $\hat{z} = 2.0$ and $\hat{z} = 5.0$ (solid lines). The dashed line always refers to the far-zone asymptote, Eq. (28).

Fig. 11. Normalized spectral energy density at the virtual source for the setup in Fig. 1(a). These profiles are shown for $\phi = 0.1$, $\phi = 1.0$, $\phi = 10.0$ and $\phi = 50.0$ (solid lines). Solid curves are calculated with the help of Eq. (35). The dotted lines show comparison with the asymptotic limit for $\phi \ll 1$, shown in Fig. 9 and calculated using Eq. (31).

Fig. 12. Normalized spectral energy density at the virtual source for the setup in Fig. 1(a) for $\phi = 50$ (enlargement of the bottom right graph in Fig. 11).

Fig. 13. $\hat{z}^2\hat{I}$ at $\phi = 50$. These profiles are shown as a function of angles at different observation distances $\hat{z} = 0.52$, $\hat{z} = 0.6$, $\hat{z} = 1.5$ and $\hat{z} = 100.0$.

Fig. 14. Transition undulator radiation geometry.

Fig. 15. Cross-check of Eq. (61) with the help of SRW. Here $L_1 = L_w = L_2 = 200$ m, $E = 17.5$ GeV, $\lambda = 400$ nm, $R = 400$ m, and $K = 3.3$. Here $\lambda_w = 3.56$ cm.

The observer is located at $z = 6000$ m. Circles represent horizontal and vertical cuts of the intensity profiles calculated numerically with SRW. The solid curve is calculated with Eq. (61). The dashed curve is obtained with the near-zone expressions Eqs. (69)-(72).

Fig. 16. Cross-check of analytical results with SRW. Here $L_1 = L_w = L_2 = 200$ m, $E = 17.5$ GeV, $\lambda = 400$ nm, $R = 400$ m, and $K = 3.3$. The observer is located at $z = 360$ m. Here $\lambda_w = 3.56$ cm. Horizontal and vertical cuts of the intensity profiles are compared with results obtained with the help of Eqs. (69) to (72).

Fig. 17. Cross-check of analytical results with SRW. Here $L_1 = L_w = L_2 = 200$ m, $E = 17.5$ GeV, $\lambda = 400$ nm, $R = 400$ m, and $K = 3.3$. Here $\lambda_w = 3.56$ cm. The observer is located at $z = 600$ m. Horizontal and vertical cuts of the intensity profiles are compared with results obtained with the help of Eqs. (69) to (72).

Fig. 18. Cross-check of analytical results with SRW. Here $L_1 = L_w = L_2 = 200$ m, $E = 17.5$ GeV, $\lambda = 400$ nm, $R = 400$ m, and $K = 3.3$. Here $\lambda_w = 3.56$ cm. The observer is located at $z = 1200$ m. Horizontal and vertical cuts of the intensity profiles are compared with results obtained with the help of Eqs. (69) to (72).